Using Convergent-Beam Techniques

21

CHAPTER PREVIEW

In the preceding chapter we described how to obtain a variety of CBED patterns under various experimental conditions, but always with a focused beam. In this chapter you will find out why these patterns are so useful: they contain a wealth of quantitative data. First, we'll show how to measure the specimen thickness. Next, we'll describe the steps for a complete crystallographic analysis of your specimen including determination of its unit cell, crystal system, point group, and space group. Then, we'll introduce you to methods of determining extremely small changes in lattice parameter which can be used to measure lattice strain and, indirectly, composition. Other convergent-beam techniques are also available, some of which use a somewhat defocused beam, as well as different microdiffraction methods which we will briefly summarize at the end of the chapter.

We should warn you at this stage that this analysis requires a very good understanding of crystallography. Both the learning and the doing are time-consuming processes. We suggest that first you skim the chapter and review your crystallography. The thickness determination described in Section 21.1 is required reading for anyone doing XEDS in the TEM.

D. B. Williams et al., *Transmission Electron Microscopy*

Using Convergent-Beam Techniques

21

21.1. THICKNESS DETERMINATION

As you read through this book you will become aware that a direct and accurate measure of the specimen thickness is essential for many aspects of TEM and AEM, such as the correction of X-ray intensities for absorption within the specimen and for determining the attainable X-ray spatial resolution (see Chapters 35 and 36). A most useful application of CBED patterns is that you can use them to measure the thickness of a crystal.

When you record a ZAP under conditions where $2\alpha_S < 2\theta_B$, such as shown in Figure 20.2B in the previous chapter, the 000 disk usually contains concentric diffuse fringes known as Kossel–Möllenstedt (K–M) fringes. If you move the specimen under the beam and it is not too bent, then you will see that the number of these fringes changes. In fact, the number of fringes increases by one every time the thickness increases by one extinction distance, ξ_g; if the specimen is less than one extinction distance thick, then you see no fringes and the 000 disk is uniformly bright, as shown back in Figure 20.6A. Clearly, these fringes contain thickness information. In fact, because the foil thickness can be measured at precisely the point you are doing diffraction and microanalysis, and because the method is very amenable to computerization, it has become a most popular use for CBED patterns. The region of the foil you select should be relatively flat and undistorted, and the beam must be focused at the plane of the specimen. The method is, of course, limited to crystalline specimens and it can be a bit tedious, but it is one of the best and, certainly for fully crystalline materials, the most accurate method of thickness determination.

In practice, to simplify the interpretation, we don't make thickness measurements under zone-axis conditions. You need to tilt to two-beam conditions with only one strongly excited *hkℓ* reflection. If you do this you will see that the CBED disks contain parallel rather than concentric intensity oscillations, as shown in Figure 21.1. If you go to thicker regions of your specimen you'll get many more fringes, and in this case it often helps to energy-filter the pattern (look ahead to Figure 40.15).

These oscillations are symmetric in the *hkℓ* disk and asymmetric in the 000 disk.

We'll see in Chapter 23 that these fringes are equivalent to the rocking-curve intensity oscillations which occur across a bend contour in a BF image. We'll also see in Chapter 23 that bend contours arise when elastic deformation bends the diffraction planes, and so an incoming parallel beam "sees" a range of scattering angles across the bent region (see Figure 21.2A). In a similar manner, when you use a convergent beam and the illuminated region is undeformed, then the convergent beam provides a range of incidence angles to the diffracting *hkℓ* planes (see Figure 21.2B). The procedure to extract the thickness from the fringe pattern was first described by Kelly *et al.* (1975) and developed in detail by Allen (1981).

If you look at the *hkℓ* disk through a 10× lupe containing a graticule, then it is easy to measure the distance between the central bright fringe and each of the dark fringes with an accuracy of about ±0.1 mm. The central bright fringe is at the exact Bragg condition where $\mathbf{s} = 0$. The fringe spacings correspond to angles $\Delta\theta_i$ as shown schematically in Figure 21.3A, and from these spacings you can obtain a deviation s_i for the ith fringe from the equation

$$s_i = \lambda \frac{\Delta\theta_i}{2\theta_B d^2} \qquad [21.1]$$

where θ_B is the Bragg angle for the diffracting *hkℓ* plane, d is the *hkℓ* interplanar spacing, and we'll use the magnitude of $\mathbf{s}$, ignoring its sign. The angle $2\theta_B$ in the CBED pattern is, of course, just the separation of the 000 and *hkℓ* disks.

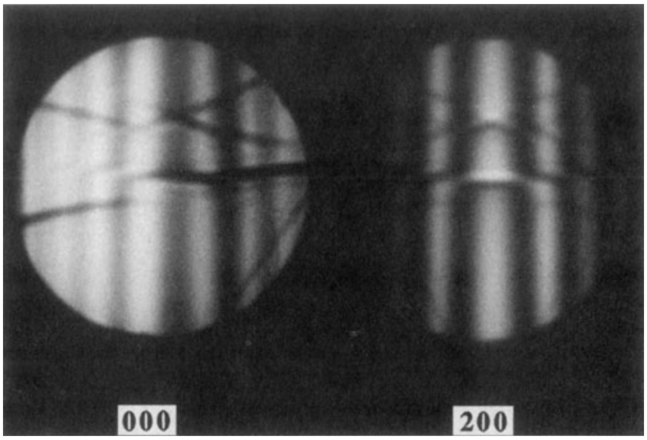

Figure 21.1. Kossel–Möllenstedt fringes in a ZOLZ CBED pattern from pure Al taken under two-beam conditions with (200) strongly excited.

The specimen in Figure 21.1 is pure Al and the 200 reflection is excited. For Al, d_{200} is 0.2021 nm. If the extinction distance ξ_g is known, then you can determine the foil thickness t since

$$\frac{s_i^2}{n_k^2} + \frac{1}{\xi_g^2 n_k^2} = \frac{1}{t^2} \qquad [21.2]$$

where n_k is an integer (k is an integer not related to λ). If you don't know ξ_g, you use a graphical method, plotting the measurements for several fringes as follows:

- Arbitrarily assign the integer $n = 1$ to the first fringe, which corresponds to an excitation error s_1.
- Then assign $n = 2$ to the second fringe, s_2, etc.
- Then plot $(s_i/n_k)^2$ versus $(1/n_k)^2$. If the result is a straight line, your arbitrary assignment was good. That is, the relationship between i and k is given by $k = i + j$, where j is the largest integer $<(t / \xi_g)$.
- If your plot is a curve, then repeat the procedure by re-assigning $n = 2$ to the first fringe.
- Continue to iterate until you find a straight line, as shown in Figure 21.3B.

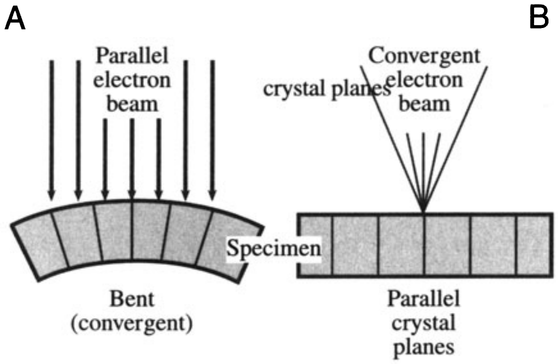

Figure 21.2. The reciprocal relationship between electron ray paths and crystal planes during (A) the formation of bend contours in BF images and (B) the formation of K–M fringes in CBED disks .

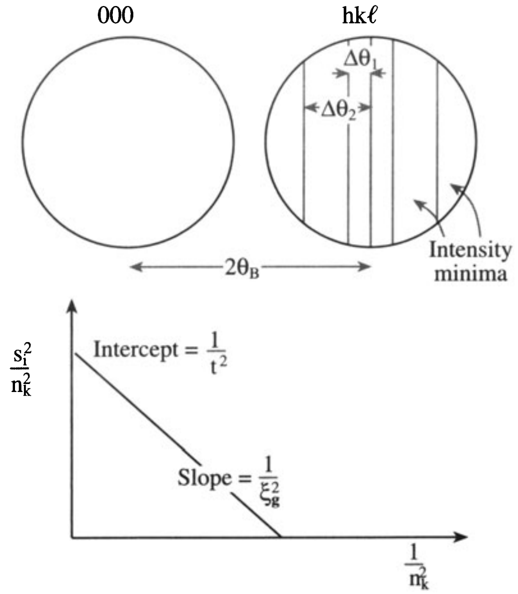

Figure 21.3. (A) The measurements necessary to extract thickness (t) from K–M fringes. From n_i measure spacings of $\Delta\theta_i$, determine the deviation parameters s_i, then (B) plot $(s_i/n_k)^2$ against n_k^2. If the plot is a straight line, extrapolate to the ordinate to find t^{-2}) and hence t.

You have to do all this because the minimum thickness may be $>\xi_g$. From the straight line plot, the intercept is t^{-2} and the slope is $-\xi_g^{-2}$. We will now go through an example in detail.

Example

■ If we apply this method to Figure 21.1, we find that the first set of values of s_i for the three dark fringes are s_1, s_2, and s_3 given in Table 21.1. Now we guess the values of n, as shown in column 2, to give the values for $(s_i/n_k)^2$ in column 3.

These data do not plot as a straight line, since both $(s_1/1)^2$ and $(s_3/3)^2$ are less than $(s_2/2)^2$. So we then assign the integer 2 to the first fringe, etc. We then find a

Table 21.1. CBED Data for Thickness Determination

s_i (nm^{-1})	n_i	s_i^2/n_i^2 (nm^{-2})
$s_1 = 0.84 \times 10^{-2}$	$n_1 = 1$	0.7×10^{-4}
$s_2 = 2.1 \times 10^{-2}$	$n_2 = 2$	1.1×10^{-4}
$s_3 = 3.0 \times 10^{-2}$	$n_3 = 3$	1.0×10^{-4}

Table 21.2. Alternative CBED Data for Thickness Determination

s_i (nm^{-1})	n_k	s_i^2/n_k^2 (nm^{-2})
$s_1 = 0.84 \times 10^{-2}$	$n_l = 2$	1.7×10^{-5}
$s_2 = 2.1 \times 10^{-2}$	$n_2 = 3$	4.9×10^{-5}
$s_3 = 3.0 \times 10^{-2}$	$n_3 = 4$	5.6×10^{-5}

second set of values as shown in Table 21.2, and these numbers plot as a straight line, as shown in Figure 21.3B. The intercept of the line with the ordinate is $1/t^2$, and this equals 6.1×10^{-5} nm^{-2}. Therefore, we find that $t^2 = (6.1)^{-1} \times 10^5$ nm^2, and so $t = 128$ nm. This procedure lends itself to computerization. It is possible to digitize the fringes on line by scanning the pattern across the STEM detector or using a CCD camera. Software is available to do this analysis; you may even want to try writing the program yourself or incorporate equation 21.2 into a spreadsheet/graphing program.

21.2. UNIT-CELL DETERMINATION

Before you start on the more esoteric aspects of crystal-structure determination, such as the analysis of point groups and space groups, you can make life much easier for yourself by determining the unit cell of your specimen (Ayer, 1989). In fact, such a determination is only possible if you already know the crystal system of the specimen. Now in TEM investigations it is rare that we look at a totally unknown specimen, and so in this chapter we'll assume that you know the crystal structure of your specimen. If, in fact, you don't know the structure, then you have to start with symmetry determination to find the point group, first of all, and then you can deduce the crystal structure. In this case then you should proceed first to Section 21.3.

We saw in the previous chapter that a CBED pattern at small L often reveals one or more rings of HOLZ intensity and you learned how to index the diffraction disks that make up these rings. If you don't know the structure, then of course it will be rather difficult to index the pattern, since you don't know the appropriate systematic absences. These rings are most useful in themselves, even if you haven't indexed the individual disks.

> If you measure the radii of the rings (G), you can deduce the lattice-repeat vector of the crystal parallel to the beam direction.

So by tilting to an orientation in which the beam is coming down an axis of the unit cell, such as [001] in an orthorhombic crystal, the disk spacings in the ZOLZ pattern will give you the [100] and [010] lattice parameters and the HOLZ-ring radius will give you [001].

Hence you should be able to determine all the lattice parameters of the unit cell in a single pattern. If you're not sure which pattern to choose, any low-index (i.e., high-symmetry) pattern is a good starting point. There are appropriate analytical expressions for calculating the spacing between atomic planes parallel to the beam and we'll discuss them next. These expressions give you the lattice parameters, since the lattice spacing is related to the lattice parameter by standard equations, given in standard crystallography texts (see Chapter 18). Then you have to look at differences between the ZOLZ and HOLZ disk patterns to determine the type of lattice centering. So you'll now learn how to utilize a unique aspect of CBED patterns, namely, that from a single two-dimensional pattern you can obtain 3D information about the crystal.

21.2.A. Experimental Considerations

The first thing you have to do is get DPs containing clear ZOLZ and HOLZ maxima. The patterns should have a small L to reveal one or more rings.

> It is good practice to record two patterns, one with a large C2 aperture (therefore large α, Kossel conditions) and one with a small C2 aperture to show the individual disks (K–M conditions).

Such a pair of patterns is shown in Figures 21.4A and B. We will use the ring pattern to measure G and the disk pattern to index individual HOLZ reflections, and observe both the relative spacings and positions of ZOLZ and HOLZ reflections.

21.2.B. The Importance of the HOLZ-Ring Radius

If you go back and look at Figures 20.7A–C you will see the simple geometrical relationship between H and G:

- H is the spacing of the reciprocal-lattice planes parallel to the electron beam.
- G_n is the projected radius of a HOLZ ring that you measure on the photograph. If the HOLZ ring is split, always measure G_n using the innermost ring.
- If the order of the ring is too large ($\alpha \sim 10°$), then your measurements may suffer from the effects of lens distortion because the scattering semiangle is so large. You must calibrate the distortion in reciprocal space using a known

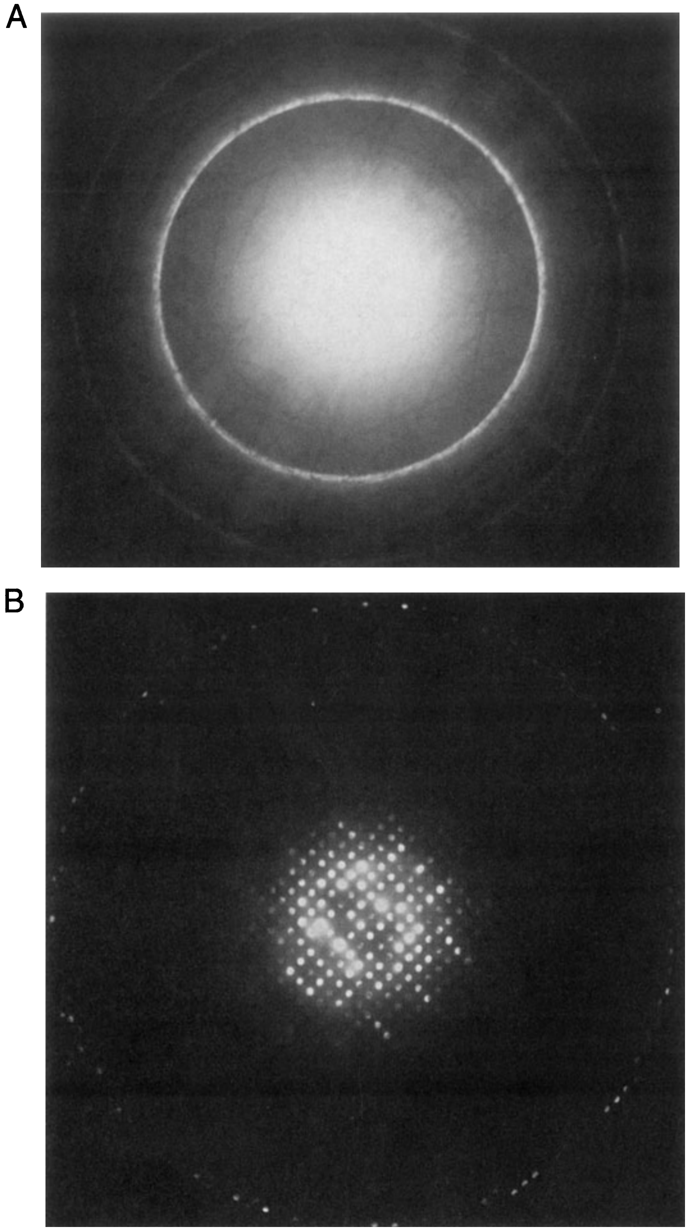

Figure 21.4. (A) CBED Kossel pattern from a carbide particle taken with a 150-µm C2 aperture showing the FOLZ ring of intensity surrounding the overexposed ZOLZ region. In (B) the same pattern, taken with a 20-µm aperture, reveals individual reflections in both the ZOLZ and FOLZ.

> specimen from which G_1, G_2, etc. can be calculated and compared with the values obtained experimentally.

Experimentally, you'll find it much easier to measure G from a Kossel pattern because the HOLZ intensity appears as one or more rings, as in Figure 21.4A. Since the radius of the Ewald sphere increases with decreasing electron wavelength λ, the value of G for any given orientation will increase as the accelerating voltage is raised, so it becomes increasingly difficult to see HOLZ rings at intermediate voltages.

From the geometry of Figure 20.7A and assuming that terms in H^2 are negligible, the radii of the FOLZ and SOLZ rings, G_1, and G_2, are (Steeds, 1979)

$$G_1 = \left(\frac{2H}{\lambda}\right)^{1/2} \qquad [21.3]$$

and

$$G_2 = 2\left(\frac{H}{\lambda}\right)^{1/2} \qquad [21.4]$$

where both G and H are in reciprocal-space units (nm^{-1} or Å^{-1}). Similar expressions can be developed, if you need them, for third- and higher-order zones. In practice, most people find it easier to think in real space, rather than reciprocal space, and so we rewrite these equations in terms of the spacing between Laue zones (H^{-1}) in real-space units. We use the inverse relationship between real and reciprocal space to give, for the FOLZ

$$\frac{1}{H} = \frac{2}{\lambda G_1^{\,2}} \qquad [21.5]$$

The value of H^{-1} can be expressed in real-space units (nm) through the measured radius r (mm) and the camera constant λL (nm mm)

$$\frac{1}{H} = \left(\frac{2}{\lambda}\right)\left(\frac{\lambda L}{r}\right)^2 \qquad [21.6]$$

You must take the time to measure λL carefully (see Section 9.6), because this will minimize errors in H^{-1} which could be quite large due to the $(\lambda L)^2$ dependence in equation 21.6. From the above equations, and from Figure 20.8, you can see that a low-symmetry zone axis with a small H will give rise to a small HOLZ ring of diameter r on the DP, which will be easier to observe at any chosen L.

Summarizing the story so far: By measuring r values, you can determine the real-lattice spacing (H^{-1}) parallel to the beam direction. The next thing to do is compare this measured value, H_m^{-1}, with calculated values, H_c^{-1}, assuming a certain unit cell. Now H^{-1} is directly related to the magnitude of the real-space direction vector

$$\frac{1}{H} = \left|[UVW]\right| \qquad [21.7]$$

and so this magnitude can be calculated for a specific beam direction $[UVW]$.

Example

For an fcc crystal (Steeds 1979)

$$\frac{1}{H} = \frac{a_0\left(U^2 + V^2 + W^2\right)^{1/2}}{p} \qquad [21.8]$$

where a_0 is the lattice parameter, $p = 1$ when $(U+V+W)$ is odd, and $p = 2$ when $(U+V+W)$ is even. For bcc crystals $p = 2$ if U, V, and W are all odd; otherwise $p = 1$. These conditions for p just take account of structure-factor effects which cause systematic absences of some reflections, or in some cases whole rings. If a whole ring is absent, the calculated reciprocal lattice layer spacing H_c^{-1} must be an integer multiple of the measured spacing H_m^{-1}. Thus

$$\frac{1}{H_c} = n\left(\frac{1}{H_m}\right) \qquad [21.9]$$

where n must be an integer. If n is nonintegral, then your indexing is wrong. A generalized method for determining which Laue zone you should see has been given by Jackson (1990). You can see that, if you have indexed the ZOLZ (i.e., $[UVW]$ is known), r is measured, and λ is known, then H can be determined without the need to index individual spots in the HOLZ ring of intensity.

It is possible to develop more generalized equations for H^{-1} than equation 21.8 (Raghavan *et al.*, 1984, Ayer, 1989).

Other examples

In a crystal system with orthogonal axes (i.e., orthorhombic, tetragonal, or cubic systems, with lattice-repeat spacings a, b, c), if there are no absences of HOLZ layers ($p = 1$) then for a given zone axis UVW

$$\frac{1}{H} = \left(a^2U^2 + b^2V^2 + c^2W^2\right)^{1/2} \qquad [21.10]$$

Similarly, for hexagonal or rhombohedral systems using a three-index system

$$\frac{1}{H} = \left(a^2\left(U^2 + V^2 - UV\right) + c^2W^2\right)^{1/2} \qquad [21.11]$$

and for the four-index system

$$\frac{1}{H} = \left(3\left(U^2 + V^2 + UV\right)^2 + c^2W\right)^{1/2} \qquad [21.12]$$

while for the monoclinic system with a unique b-axis

$$\frac{1}{H} = \left(U^2a^2 + V^2b^2 + W^2c^2 + 2UWac\cos\beta^2\right)^{1/2} \qquad [21.13]$$

If you are working with a low-index, high-symmetry zone axis it may be just as easy to determine H^{-1} directly from reciprocal lattice constructions rather than using equations. However, for less symmetrical crystallographic directions, such constructions are effectively impossible to visualize and then you should use these equations.

So, in summary, we can give some guidelines:

- Measure the radius of the HOLZ ring to give a value of the reciprocal of the spacing between the HOLZ and the ZOLZ, H_m^{-1}.
- Compare the measured spacing with the spacing calculated assuming a given unit cell, H_c^{-1}.
- The measured value should agree with, or be a multiple of, the calculated value. For example, if given a square ZOLZ DP, you assume a cubic crystal, then the unit-cell repeat vector should be identical in all three dimensions, and so the FOLZ-ring diameter should give the same value of H^{-1} as that determined from the other two axes from the square [100] pattern. If H^{-1} is different, then the crystal is not cubic but another system, such as tetragonal.

21.2.C. Determining the Lattice Centering

When you have measured H^{-1} from the Kossel pattern, the next thing to do is to compare the ZOLZ and FOLZ reflections in the K–M pattern obtained with a small C2 aperture, such as Figure 21.4B. The superposition of the FOLZ and ZOLZ gives you information on the type of lattice you are dealing with, since centered lattices of all types will give different superposition patterns compared with a primitive lattice.

In the primitive lattice of Figure 21.5, the FOLZ superimposes directly on the ZOLZ because there are no systematic absences. However, face-centered and body-centered lattices will give rise to displacements of the FOLZ pattern with respect to the ZOLZ in certain beam directions, as shown by Hirsch *et al.* (1977) and illustrated schematically in Figure 21.5A. You can quite easily work out the displacement in terms of a shift vector for cubic crystal patterns in low-index orientations and we showed examples back in Figures 20.9 and 20.10. It is not so simple in more complex crystals, but Jackson (1987) has developed a generalized method of determining the shift vector **t** for all crystal systems and all orientations

$$\mathbf{t} = \mathbf{g} - \mathbf{u}^*\left(\frac{HN_\mathrm{L}}{|\mathbf{u}^*|}\right) \qquad [21.14]$$

where **g** is the vector for the $hk\ell$ HOLZ reflection, $\mathbf{u}^*$ is the vector normal to the ZOLZ and parallel to H, and N_L is the number of the Laue zone containing $hk\ell$. To determine **t**, then all you do is look up values of H, $\mathbf{u}^*$, and $H/|\mathbf{u}^*|$, tabulated by Jackson (1987).

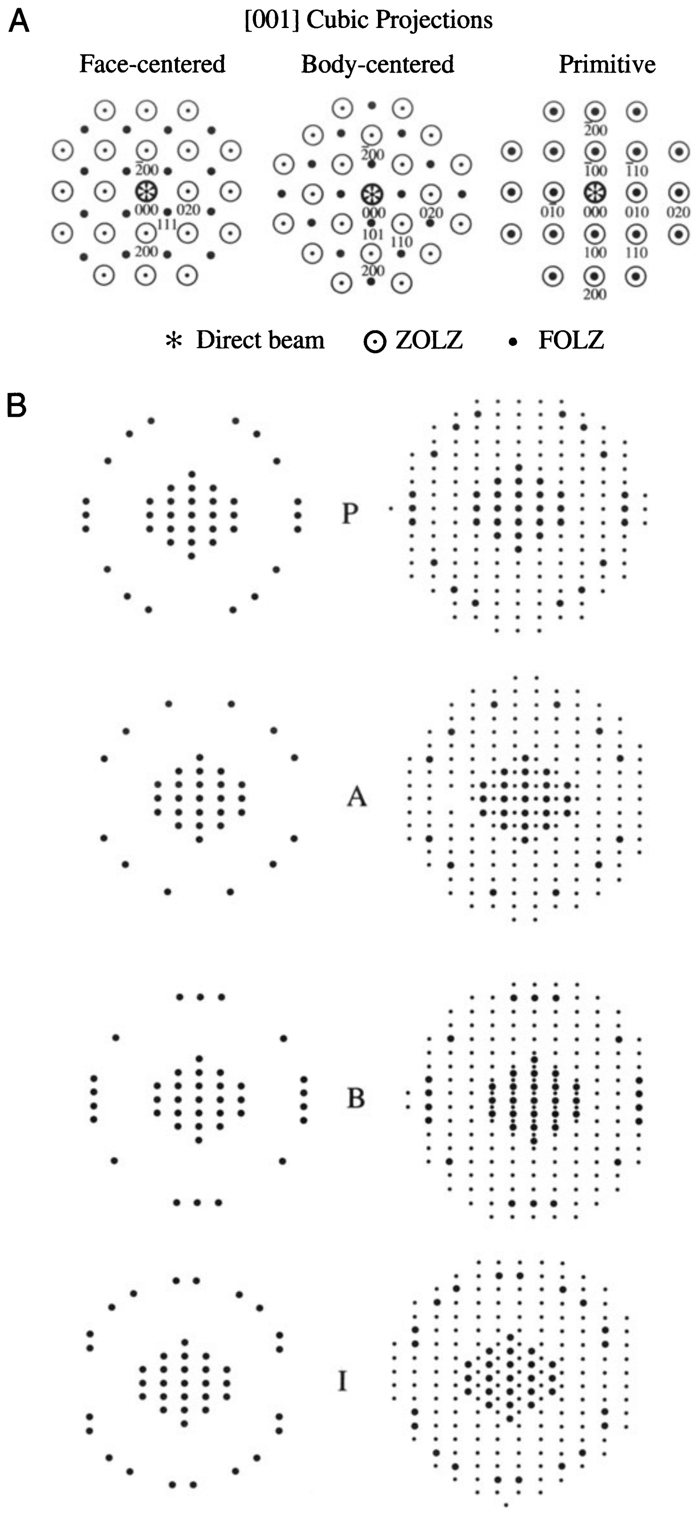

Figure 21.5. (A) The overlap between the ZOLZ and the FOLZ when looking down the [001] axis of cubic crystals. In the fcc pattern, 111 is a FOLZ index, likewise 101 in bcc. In the primitive pattern, only the ZOLZ is indexed. (B) Schematic illustration of the superposition of the FOLZ pattern on the ZOLZ pattern for an orthorhombic crystal with the electron beam down [001], showing the differences in the superposition for (P) primitive, (A) A-centered, (B) B-centered, and (I) I-centered lattices.

Example

We can illustrate the shift due to lattice type, by looking at Figure 21.5B, which is a series of schematic patterns for an orthorhombic cell (Ayer 1989) oriented along the [001] axis. In each pattern the experimentally observed distribution of ZOLZ and FOLZ reflections is shown and adjacent to it is the same pattern but containing the FOLZ reciprocal-lattice points. So the FOLZ ring of spots is always coincident with the FOLZ reciprocal-lattice points. In the top pattern (P) the ZOLZ and FOLZ superimpose exactly and this would be the case for a primitive unit cell. In (A) the FOLZ lattice is displaced from the ZOLZ reflections by half the spacing of the ZOLZ reciprocal-lattice points in the [010] direction; this is the situation expected for an A-face-centered lattice. The next two patterns (B and I) show the expected displacements for a B-face-centered and an I (body-centered) lattice.

So you now know how to measure the lattice-repeat vectors in three dimensions and determine the type of lattice centering. This information should be sufficient to allow you to determine the correct unit cell of your specimen, particularly if you have further information such as chemical analysis by XEDS or EELS.

21.3. SYMMETRY DETERMINATION

21.3.A. Introduction to Symmetry Concepts

Before you study the following two sections you must have a basic understanding of crystal-symmetry elements (both rotational and translational) and be familiar with the standard international notation for point groups and space groups. You will also need to know how to represent the point-group symmetry of a crystal using the stereographic projection we discussed in Section 18.4. In Figure 21.6 we reproduce the standard point-group table familiar to any student of crystallography; we will refer to this table again. If you aren't familiar with such concepts, then the rest of this section may be incomprehensible and you should go and read one of the crystallography texts which we listed at the end of Chapter 18.

> The crystallographic point groups are the sets of crystallographically permissible symmetries which are formed when sets of axes intersect in a common point. The axes correspond to the rotation, inversion, and mirror symmetry elements. We generally choose our lattice points to have a particularly high degree of symmetry. We will ignore translational symmetry elements until we discuss space groups.

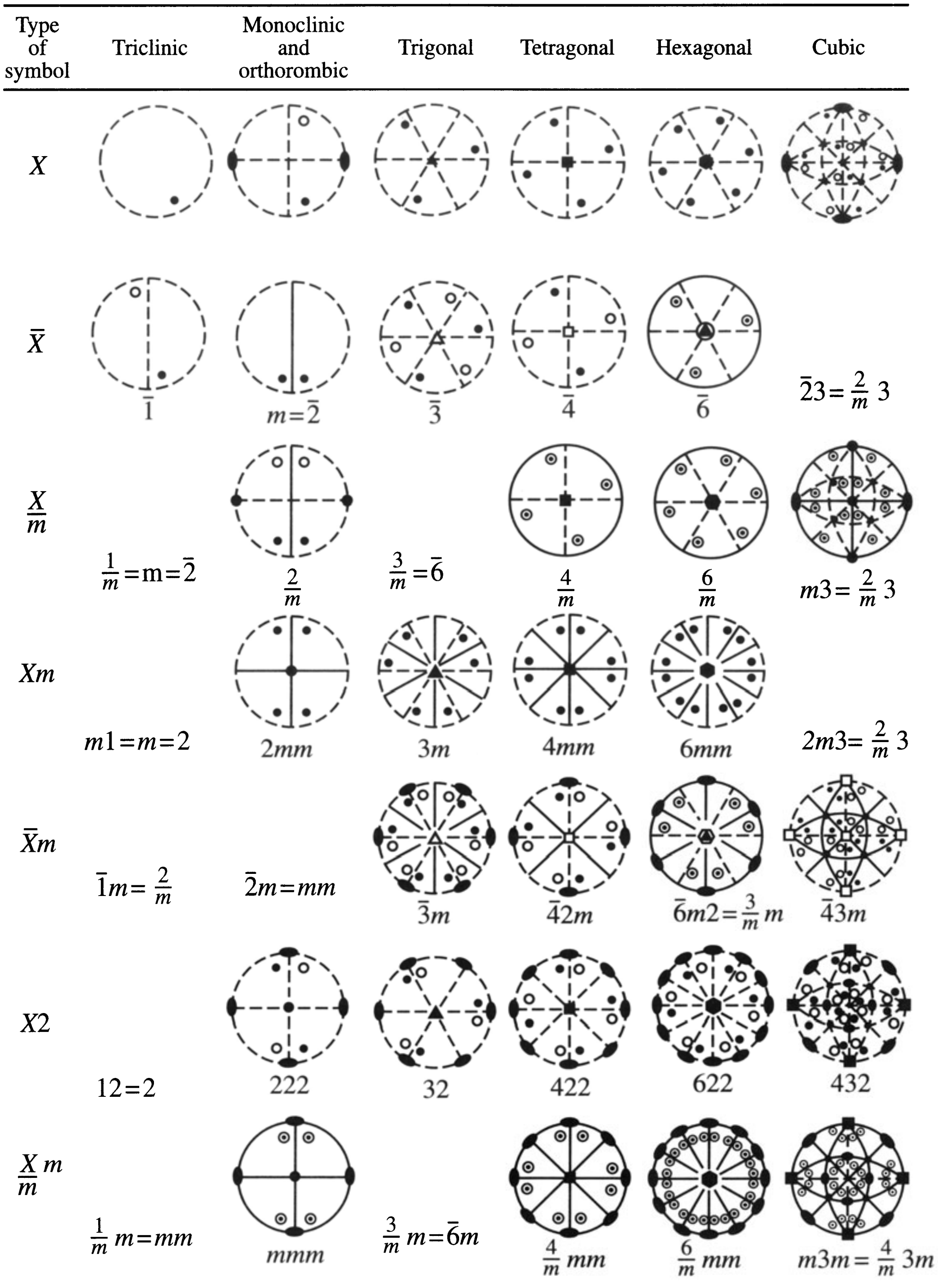

Figure 21.6. The 32 crystal point groups represented by stereograms showing the operation of rotational, mirror, and inversion symmetry elements on a general pole *hkℓ*. The international notation describing the point groups is given under each of the stereograms.

Historically, point-group determination has been the domain of X-ray crystallographers and electron microscopists have gladly avoided such concepts. However, the point group is not only useful for classifying crystals with common symmetry elements, but it is also an important indicator of many of the properties of the crystal, such as anisotropy in the electrical resistivity or the refractive index. With the availability of CBED you can now determine the point group of a thin crystal directly in the TEM, simply by recording two or three low-index ZAPs.

This process has a tremendous advantage over classical X-ray techniques because:

- We obtain this information from much smaller regions than is possible using X-rays.
- We can also distinguish all 32 possible point groups unambiguously, which is a nontrivial process using X-rays.

So as an electron microscopist you must now master the details of point-group determination if you are to take full advantage of the capabilities of a modern TEM. You'll see that it's not too difficult an exercise, but there is no escaping the need to comprehend some of the basic principles of crystal symmetry. The exercises will require quite a lot of careful work and time. Therefore, if you can uniquely identify the unknown phase in your specimen through some other technique such as XEDS or EELS, do so.

21.3.B. Friedel's Law

Symmetry determination in crystals has evolved from the early work of Friedel and von Laue on the kinematical theory of X-ray diffraction. We can summarize a fundamental aspect of Friedel's work as follows.

> *Friedel's Law:* The intensity of some reflection $hk\ell$ in an X-ray DP is equal to the intensity in its opposite reflection $\bar{h}\bar{k}\bar{\ell}$.

If this is so, a center of symmetry exists in the DP. This is the case for most X-ray DPs from single crystals, because most X-ray diffraction occurs under kinematical conditions.

> The presence of a mirror plane in a crystal, parallel to axes *a* and *b*, makes the intensity of all reflections of type $hk\ell$ equal to the intensity of the corresponding $\bar{h}\bar{k}\bar{\ell}$ reflection.

So, under kinematical-diffraction conditions, we cannot readily distinguish a mirror plane from a twofold rotational axis (diad) parallel to the mirror plane. That is equivalent to saying that (see Figure 21.6) *we cannot distinguish point groups* m *and 2*. Similarly, the presence of a fourfold rotation axis (tetrad) in a crystal, parallel to the *c*-axis, results in $I_{hk\ell} = I_{k\bar{h}\ell} = I_{\bar{h}\bar{k}\ell} = I_{\bar{k}h\ell}$, where $I_{hk\ell}$ denotes the diffracted intensity of a reflection of type $hk\ell$. Under kinematical conditions, these intensities are also the same as $I_{hk\bar{\ell}} = I_{\bar{k}h\bar{\ell}} = I_{\bar{h}\bar{k}\bar{\ell}} = I_{k\bar{h}\bar{\ell}}$.

X-ray diffraction is thus severely limited for point-group determination because of Friedel's law. Since crystals which do not possess true centers of symmetry (noncentrosymmetric crystals) still appear in X-ray DPs to possess a center of symmetry, they cannot be readily distinguished from centrosymmetric crystals. If you go back and look at the 32 point groups in Figure 21.6 and remove all those which do not contain a center of symmetry, then you are left with only 11 centrosymmetric point groups: $\bar{1}$, 2/*m* (equivalent to *mm*), *mmm*, $\bar{3}$, $\bar{3}m$, 4/*m*, 4/*mmm*, 6/*m*, 6/*mmm*, *m*3, and *m*3*m*. These are known as the *Laue groups* in X-ray diffraction. Except under "anomalous" scattering conditions, X-ray diffraction can only determine these 11 symmetry groups.

> In CBED patterns, *Friedel's law* breaks down because of dynamical scattering.

So, to get the full symmetry information, the crystal must be thick enough for you to see dynamical-diffraction contrast within the CBED disks. If you then examine the intensity distributions within individual $hk\ell$ reflections, you can distinguish centrosymmetric and noncentrosymmetric crystals. That is, the 32 crystal point groups are not reduced to the 11 Laue groups, as occurs in X-ray diffraction.

21.3.C. Looking for Symmetry in Your Patterns

Before we go into details of point-group determination, let's first get some practice at looking at CBED patterns and seeing the symmetry within them. When we look at CBED pattern symmetry we use the same notation as for point groups, i.e., a number *X* (=1, 2, 3, 4, or 6) for a rotation axis and *m* for a mirror plane parallel to the rotation axis, and a second *m* for any independent mirror plane. Inversion symmetry or a mirror normal to the beam direction cannot be discerned and so the terms of the form $\bar{X}$ or *X*/*m* are not used. The only combinations we can get are the same as for the ten two-dimensional point groups: 1, 2, *m*, 2*mm*, 3, 3*m*, 4, 4*mm*, 6, or 6*mm*. These symbols refer to the observable symmetry in the pattern, and four examples of different pattern symmetries are shown schematically in Figure 21.7.

Symmetry determination is always carried out using ZAPs:

- You may find it easier to do the final adjustments to get an exact ZAP using the beam-tilt/shift controls.
- As a last resort you may have to displace the C2 aperture slightly off axis to center it precisely around the center of symmetry in the ZAP.

There are two specific kinds of symmetry that you have to look for in CBED patterns:

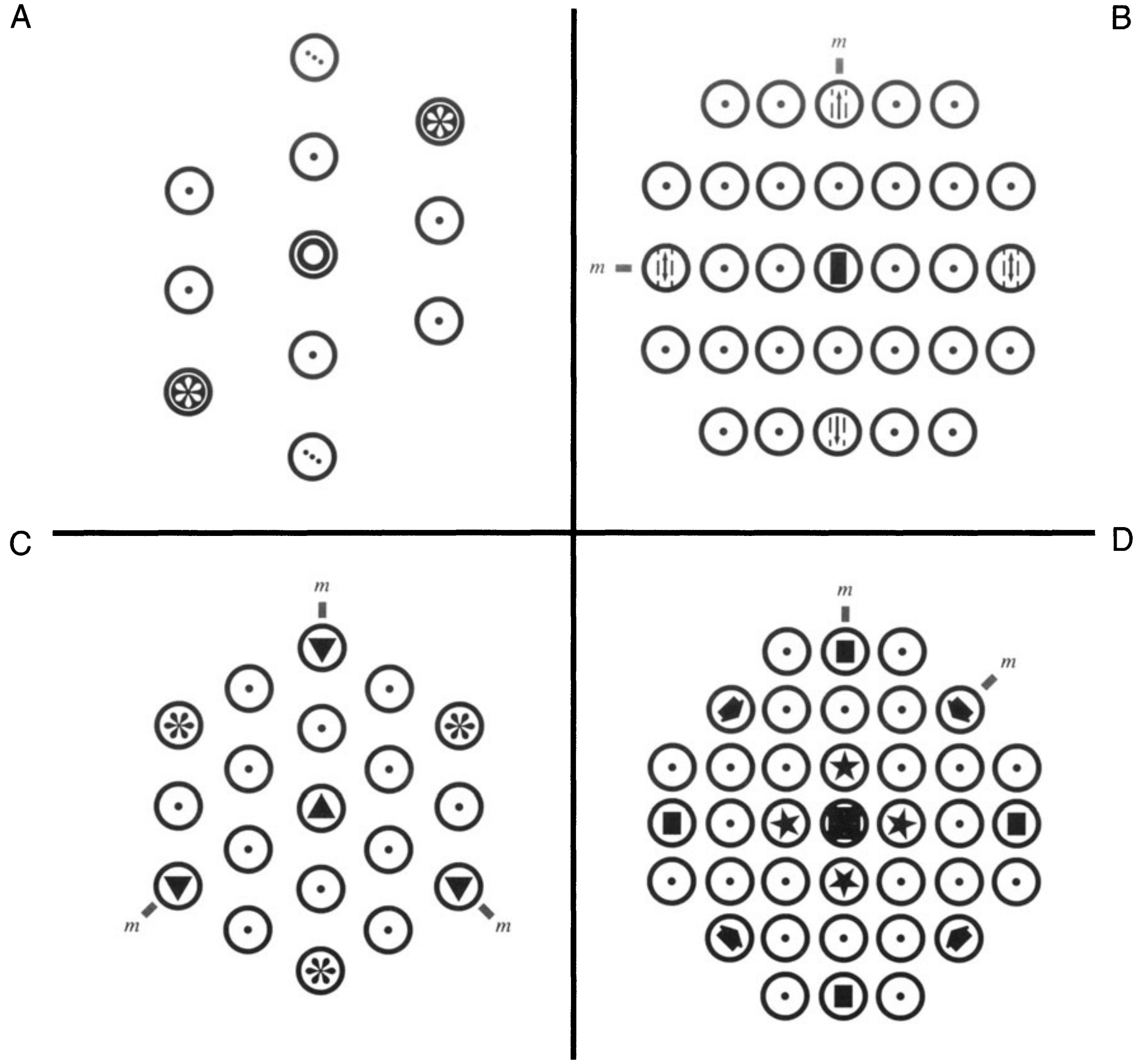

Figure 21.7. Four examples of symmetry in CBED patterns. (A) Symmetry 2 refers to a twofold (diad) rotation axis, i.e., the pattern has symmetry when rotated 180°; (B) 2*mm* is a diad symmetry with two independent mirror planes parallel to the diad; (C) 3*m* indicates threefold rotation (triad) symmetry with one mirror plane, i.e., rotational symmetry every 120° with one mirror plane present at each 120°; (D) 4*mm* indicates a fourfold rotational symmetry (tetrad) with two independent mirror planes parallel to the tetrad.

- Whole-pattern (WP) symmetry.
- Bright-field (BF) symmetry.

The first and most important is the *WP symmetry*. The WP symmetry is just what it says; the symmetry of the complete pattern, including the relative positions of the HOLZ reflections and any HOLZ Kikuchi lines. To be sure you get the correct symmetry, you should take a small camera-length pattern to include the HOLZ rings since HOLZ effects are not always visible in the ZOLZ. The pattern can be either a Kossel or a K–M pattern. The WP symmetry at any orientation must belong to one of the ten two-dimensional groups listed above. If you look at the CBED pattern from Cu back in Figure 20.16, the WP symmetry is 3*m* because the HOLZ ring and the array of HOLZ-deficient Kikuchi lines shows threefold symmetry with one mirror plane reproduced every 120°. As a useful exercise look at a few other CBED patterns in this chapter and work out the WP symmetry.

The second kind of symmetry is the *BF symmetry,* which refers to the symmetry of the 000 disk only, *when HOLZ lines are present.* In this case, the BF symmetry also contains 3D information. Take care to ensure that the C2 aperture is small enough so that you can see the 000 disk without any overlap from the diffracted maxima. For example, the 000 disk back in Figure 20.2B has an array of deficient HOLZ lines which displays 3*m* symmetry.

If there is only 2D diffuse intensity within the disk, or if you ignore the HOLZ lines, then the symmetry is more correctly called the BF projection symmetry. The symmetry in either of these latter cases should again be classified into one of the ten two-dimensional point groups just listed. We will see that combination of the WP and BF symmetry in three ZAPs is usually sufficient to determine the point group.

On some occasions the projection-diffraction symmetry may be all that is available. This term refers to the symmetry displayed by the intensity in the direct 000 beam plus the *hkℓ* diffracted beams in the zero layer. It *ignores any contributions from HOLZ layers* such as HOLZ lines and HOLZ reflections, but includes any diffuse intensity within the ZOLZ disks. This is because the diffuse contrast within these disks arises from dynamical interactions within the zero layer of the crystal that give rise to K–M fringes, which we used for thickness determination. The projection-diffraction symmetry corresponds to the projected two-dimensional symmetry of the crystal down the zone axis that you have selected. The projection-diffraction symmetry is simply the symmetry displayed in SAD patterns. Since this symmetry is only two-dimensional, it is not as useful as the WP and BF symmetry. If you go back and examine Figure 20.16, the projection-diffraction symmetry is not clear because the ZOLZ disks overlap, but the ZOLZ Kikuchi bands can also be used and they show a sixfold rotational symmetry with two independent mirror planes, one within the Kikuchi bands and one between them, giving *6mm* symmetry. Similar symmetry is shown in the SAD pattern from Si in Figure 20.2A.

21.3.D. Point-Group Determination

There are several methods to determine the point group by examining the various symmetry aspects as we have just described, but the easiest method is based on the work of Steeds (1979). This method uses several different ZAPs. For each of these you have to determine the BF and WP symmetries, and ensure that they are consistent with the projection symmetry. To do this we make use of a standard table, which is given here as Table 21.3. This table is a modified version of the original table developed by Buxton *et al.* (1976) in a seminal but rather complex paper.

> The new concept introduced in these tables is the idea of the "*diffraction group*" of a crystal. This term describes the full 3D symmetry of a DP and the "*projection-diffraction group*" describes the full two-dimensional symmetry.

There are 10 two-dimensional projection-diffraction groups which are related to the 10 two-dimensional point group symbols with the addition of the symbol 1_R. 1_R denotes a rotational symmetry present in all diffraction disks around the central point of the *hkℓ* disk where the Bragg condition is satisfied. The 31 diffraction groups are obtained by combinations of the 10 two-dimensional point group symbols with the rotational symmetry, 1_R, and mirror rotations, m_R. All these groups are listed in column 1 of Table 21.3. You don't have to understand the *derivation* of the nomenclature in order to be able to carry out point group determination, but if you want to pursue the concepts in more depth, the reviews by Steeds (1984) and Tanaka (1989) may help.

The Procedure: From your ZAP, determine the BF and WP symmetry. Go to Table 21.3 and see which of the 31 possible diffraction groups accounts for the observed symmetry. There may be only one, but more often there are two possibilities. For example, if your BF and WP symmetries are $3m$ as we found for the Cu pattern, then possible diffraction groups are $3m$ or 6_Rmm_R. However, if your BF symmetry is $3m$, but the WP symmetry is only 3, then the only possible diffraction group is $3m_R$. If your patterns only contain two-dimensional information, then you may only be able to determine the projection-diffraction group, not the full diffraction group. Under these circumstances, you must go to experimental conditions that give 3D information, i.e., a thicker specimen, a shorter L to see any HOLZ rings, or cool the specimen to enhance HOLZ effects and so on, as we described in Chapter 20.

Repeat the Procedure: Conduct the same type of analysis for up to three orientations in your crystal. Remember that if you can't see the HOLZ contrast in the BF disk, you should choose a lower-symmetry orientation. When you have found the possible diffraction groups for each orientation, the crystal point group can be deduced using Table 21.4, again taken from the pioneering work of Buxton *et al.* (1976). Table 21.4 contains the 31 diffraction groups and the 32 crystal point groups. The diffraction groups, consistent with particular crystal point groups, can be deduced. For each crystal orientation and diffraction group, one or more different crystal point groups are possible. For example, the diffraction group $3m$, which is one of the two possible ones for the Cu pattern, is consistent with point groups $3m$ and $\bar{4}3m$. If you repeat this exercise for three different ZAPs, you will find that only one crystal point group is consistent with all the diffraction groups observed; this is the true point group of your specimen.

Example

Point-group determination in this manner is shown in Figure 21.8, which contains three sets of CBED patterns from three separate zone axes in austenitic stainless steel. The BF and WP symmetries are always identical in this case, although this is not in-

Table 21.3. CBED Pattern Symmetries

			Dark Field		$\pm G$		
Diffraction Group	Bright Field	Whole Pattern	General	Special	General	Special[a]	Projection-Diffraction Group
1	1	1	1	none	1	none	1_R
1_R	2	1	2	none	1	none	1_R
2	2	2	1	none	2	none	21_R
2_R	1	1	1	none	2_R	none	21_R
21_R	2	2	2	none	21_R	none	21_R
m_R	m	1	1	m	1	m_R	$m1_R$
m	m	m	1	m	1	m	$m1_R$
$m1_R$	$2mm$	m	2	$2mm$	1	$m1_R$	$m1_R$
$2m_Rm_R$	$2mm$	2	1	m	2	—	$2mm1_R$
$2mm$	$2mm$	$2mm$	1	m	2	—	$2mm1_R$
2_Rmm_R	m	m	1	m	2_R	—	$2mm1_R$
$2mm1_R$	$2mm$	$2mm$	2	$2mm$	21_R	—	$2mm1_R$
4	4	4	1	none	2	none	41_R
4_R	4	2	1	none	2	none	41_R
41_R	4	4	2	none	21_R	none	41_R
$4m_Rm_R$	$4mm$	4	1	m	2	—	$4mm1_R$
$4mm$	$4mm$	$4mm$	1	m	2	—	$4mm1_R$
4_Rmm_R	$4mm$	$2mm$	1	m	2	—	$4mm1_R$
$4mm1_R$	$4mm$	$4mm$	2	$2mm$	21_R	—	$4mm1_R$
3	3	3	1	none	1	none	31_R
31_R	6	3	2	none	1	none	31_R
$3m_R$	$3m$	3	1	m	1	m_R	$3m1_R$
$3m$	$3m$	$3m$	1	m	1	m	$3m1_R$
$3m1_R$	$6mm$	$3m$	2	$2mm$	1	$m1_R$	$3m1_R$
6	6	6	1	none	2	none	61_R
6_R	3	3	1	none	2_R	none	61_R
61_R	6	6	2	none	21_R	none	61_R
$6m_Rm_R$	$6mm$	6	1	m	2	—	$6mm1_R$
$6mm$	$6mm$	$6mm$	1	m	2	—	$6mm1_R$
6_Rmm_R	$3m$	$3m$	1	m	2_R	—	$6mm1_R$
$6mm1_R$	$6mm$	$6mm$	2	$2mm$	21_R	—	$6mm1_R$

[a] Where a dash appears, the special symmetries can be deduced from columns 5 and 6 of this table (or from Table 1 in Buxton *et al.* 1976).

variably so, as you can see from Table 21.3. The symmetries are $3m$ from the [111], $4mm$ from the [100], and $2mm$ from the [110] patterns, respectively. The diffraction group symmetry consistent with each of the three patterns can then be determined from Table 21.3. Table 21.5 lists the possible point groups consistent with the diffraction group symmetry, taken from Table 21.4, and it is immediately apparent that only one point group, $m3m$, is consistent with the symmetry in all three patterns. This conclusion can be checked by reference to Table 21.6, also from Buxton *et al.*, in which it is seen that the symmetries consistent with the $m3m$ point group are correct, i.e., 6_Rmm_R for [111], $4mm1_R$ for [100], and $2mm1_R$ for [110].

So let's summarize this detailed, but nonetheless straightforward process to determine point-group symmetry:

- Obtain at least three low-index ZAPs, and record a small camera-length pattern and large camera-length pattern at each orientation.
- From the small-*L* pattern determine the WP symmetry.
- From the large-*L* pattern determine the BF symmetry.
- From Table 21.3 determine the possible diffraction groups consistent with the WP and BF symmetries.
- From Table 21.4 determine the possible point groups and find the one consistent with your pattern symmetries in all orientations.
- If necessary, cross-check with Table 21.6 to see that the diffraction group symmetries at each orientation were consistent with the point group you deduced.

Table 21.4. Relation Between the Diffraction Groups and the Crystal Point Groups

Diffraction Group																																
$6mm1_R$																											X					
$3m1_R$																										X						
$6mm$																									X							
$6m_Rm_R$																								X								
61_R																							X									
31_R																						X										
6																					X											
6_Rmm_R																				X												X
$3m$																			X												X	
$3m_R$																		X												X		
6_R																	X												X			
3																X												X				
$4mm1_R$															X																	X
4_Rmm_R														X																	X	
$4mm$													X																			
$4m_Rm_R$												X																		X		
41_R											X																					
4_R										X																						
4									X																							
$2mm1_R$								X							X												X		X			X
2_Rmm_R					X			X			X				X					X			X				X		X			X
$2mm$							X																			X						
$2m_Rm_R$						X						X		X										X				X		X		
$m1_R$							X						X	X											X	X					X	
m				X			X						X	X					X			X			X	X					X	
m_R			X			X	X		X	X		X	X	X				X			X			X	X	X		X		X	X	
21_R					X															X												
2_R		X			X			X			X				X		X			X			X				X		X			X
2			X															X														
1_R				X															X													
1	X		X	X		X	X		X	X		X	X	X		X		X	X		X	X		X	X	X		X		X	X	
Point Group	1	$\bar{1}$	2	m	$2/m$	222	$mm2$	mmm	4	$\bar{4}$	$4/m$	422	$4mm$	$\bar{4}2m$	$4/mmm$	3	$\bar{3}$	32	$3m$	$\bar{3}m$	6	$\bar{6}$	$6/m$	622	$6mm$	$\bar{6}m2$	$6/mmm$	23	$m3$	432	$\bar{4}3m$	$m3m$

There are other methods to determine the point group symmetry, especially that discussed by Tanaka (1989). If you want to be a dedicated electron crystallographer you should become familiar with all the methods, but we haven't the space here to go into them all. We will now go on briefly to discuss the way in which we can get the space group of the crystal if the point-group identification is not sufficient to identify the unknown sample unambiguously.

21.3.E. Space-Group Determination

For a full crystallographic analysis of your specimen, you should determine the space group.

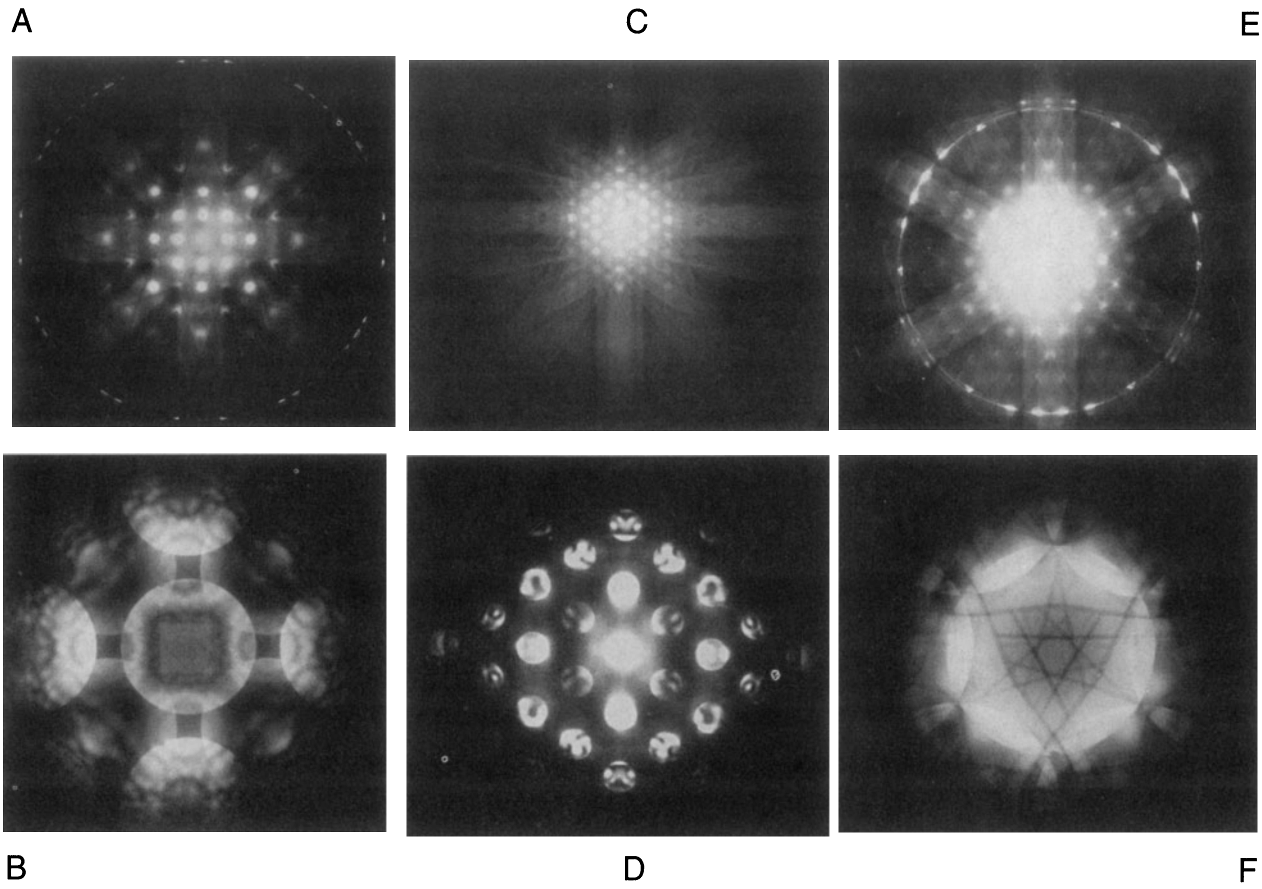

Figure 21.8. (A, B) [100], (C, D) [110], and (E, F) [111] ZAPs from stainless steel used to determine the point group. In (A, C, E) the low-*L* pattern gives the WP symmetry and in (B, D, F) the high-*L* pattern shows the BF symmetry. From the WP and BF symmetries, possible diffraction groups and point groups are determined, as summarized in Table 21.5.

> The space group is a classification of the complete symmetry of a crystal that takes into account translational symmetry elements such as glide planes and screw axes, in addition to the point symmetry elements.

The space-group notation combines the Bravais lattice type, such as primitive (P) or body-centered (I), with the point-group notation (e.g., *mmm* or 4/*mmm*) along with appropriate symbols for glide planes and screw axes, if necessary. The space group is the ultimate classification step and there are 230 possible space groups. So it is possible to be much more precise about grouping your crystal. However, knowing the space group of your crystal doesn't tell you anything more about its properties than you may have learned from knowing its point group. So there is nothing to be gained by pursuing space-group analysis if,

Table 21.5. Possible Diffraction Groups and Point Groups

Zone Axis	BF Symmetry	WP Symmetry	Possible Diffraction Groups	Possible Point Groups										
<111>	$3m$	$3m$	$3m$	$3m$	$\bar{4}3m$									
			6_Rmm_R			$\bar{3}m$	$m3m$							
<100>	$4mm$	$4mm$	$4mm$					$4mm$						
			$4mm1_R$				$m3m$		$4/mmm$					
<110>	$2mm$	$2mm$	$2mm$							$mm2$	$\bar{6}m2$			
			$2mm1_R$				$m3m$		$4/mmm$			mmm	432	$6/mmm$

Table 21.6. Zone-axis Symmetries

point group	<111>	<100>	<110>	<*UV*0>	<*UUW*>	[*UVW*]
$m3m$	$6_R mm_R$	$4mm1_R$	$2mm1_R$	$2_R mm_R$	$2_R mm_R$	2_R
$\bar{4}3m$	$3m$	$4_R mm_R$	$m1_R$	m_R	m	1
432	$3m_R$	$4m_R m_R$	$2m_R m_R$	m_R	m_R	1

point group	<111>	<100>	<*UV*0>	[*UVW*]
$m3$	6_R	$2mm1_R$	$2_R mm_R$	2_R
23	3	$2m_R m_R$	m_R	1

point group	[0001]	$\langle 11\bar{2}0\rangle$	$\langle 1\bar{1}00\rangle$	[*UV*.0]	[*UU*.*W*]	$[U\bar{U}.W]$	[*UV*.*W*]
$6/mmm$	$6mm1_R$	$2mm1_R$	$2mm1_R$	$2_R mm_R$	$2_R mm_R$	$2_R mm_R$	2_R
$\bar{6}m2$	$3m1_R$	$m1_R$	$2mm$	m	m_R	m	1
$6mm$	$6mm$	$m1_R$	$m1_R$	m_R	m	m	1
622	$6m_R m_R$	$2m_R m_R$	$2m_R m_R$	m_R	m_R	m_R	1

point group	[0001]	[*UV*.0]	[*UV*.*W*]
$6/m$	61_R	$2_R mm_R$	2_R
$\bar{6}$	31_R	m	1
6	6	m_R	1

point group	[0001]	$\langle 11\bar{2}0\rangle$	$[U\bar{U}.W]$	[*UV*.*W*]
$\bar{3}m$	$6_R mm_R$	21_R	$2_R mm_R$	2_R
$3m$	$3m$	1_R	m	1
32	$3m_R$	2	m_R	1

point group	[0001]	[*UV*.*W*]
$\bar{3}$	6_R	2_R
3	3	1

point group	[001]	<100>	<110>	[*U*0*W*]	[*UV*0]	[*UUW*]	[*UVW*]
$4/mmm$	$4mm1_R$	$2mm1_R$	$2mm1_R$	$2_R mm_R$	$2_R mm_R$	$2_R mm_R$	2_R
$\bar{4}2m$	$4_R mm_R$	$2m_R m_R$	$m1_R$	m_R	m_R	m	1
$4mm$	$4mm$	$m1_R$	$m1_R$	m	m_R	m	1
422	$4m_R m_R$	$2m_R m_R$	$2m_R m_R$	m_R	m_R	m_R	1

point group	[001]	[*UV*0]	[*UVW*]
$4/m$	41_R	$2_R mm_R$	2_R
$\bar{4}$	4_R	m_R	1
4	4	m_R	1

point group	[001]	<100>	[*U*0*W*]	[*UV*0]	[*UVW*]
mmm	$2mm1_R$	$2mm1_R$	$2_R mm_R$	$2_R mm_R$	2_R
$mm2$	$2mm$	$m1_R$	m	m_R	1
222	$2m_R m_R$	$2m_R m_R$	m_R	m_R	1

point group	[010]	[*U*0*W*]	[*UVW*]
$2/m$	21_R	$2_R mm_R$	2_R
m	1_R	m	1
2	2	m_R	1

point group	[*UVW*]
$\bar{1}$	2_R
1	1

from the point group and any other data such as XEDS or EELS, you are able to identify the crystal unambiguously. Space-group analysis is only necessary if the point group determination still leaves some uncertainty as to the nature of your crystal.

There may be some uncertainty, because even when you have determined the crystal point group and you know the lattice type, several different space groups are still possible. The next step in CBED analysis is to analyze the reflections which are kinematically forbidden (see Section 16.9) for each possible space group, and thus identify the specific space group of the crystal. Due to the dynamical nature of electron diffraction, reflections which are forbidden in kinematical diffraction often occur in CBED patterns by double diffraction. Kinematically forbidden reflections can occur by double diffraction when they are due to additional symmetry elements such as glide planes or screw axes.

> It is these translational symmetry elements which uniquely identify the space group of the crystal.

In CBED we are interested in the kinematically forbidden reflections that occur due to these additional symmetry elements. When two or more equivalent double-diffraction paths exist in a given orientation, the kinematically forbidden reflection that occurs will have a central line of zero intensity passing through the disk. These so-called dynamical absences occur in these reflections because the diffracted beams from two equivalent paths undergo complete destructive interference along the central line of the disk to which the beams are perpendicular, as shown in Figure 21.9. First, you must obtain a ZAP since the dynamical absences don't occur if the crystal is tilted off the zone. The kinematically forbidden reflections, which generally have multiple double-diffraction routes, usually lie along systematic rows of reflections, and occur in *alternate* reflections along a systematic row. You can easily distinguish the lines of absence from other contrast phenomena because they occur for all specimen thicknesses, at all values of kV, and they become narrower as the thickness increases.

The existence of a dynamical absence in a kinematically forbidden reflection indicates that the electron beam is aligned either parallel to a glide plane or perpendicular to a screw axis in the crystal. Steeds and Vincent (1983) established tables, based on the earlier work of Gjønnes and Moodie (1965), which describe the relationship between the dynamical absences and the number of symmetry elements that can be responsible for those absences. These relationships, shown in Table 21.7, are used for interpreting the presence of screw axes and glide planes in space-group determinations using 3D CBED effects. Some rare situations exist where this approach breaks down but, in general, it has withstood the test of time.

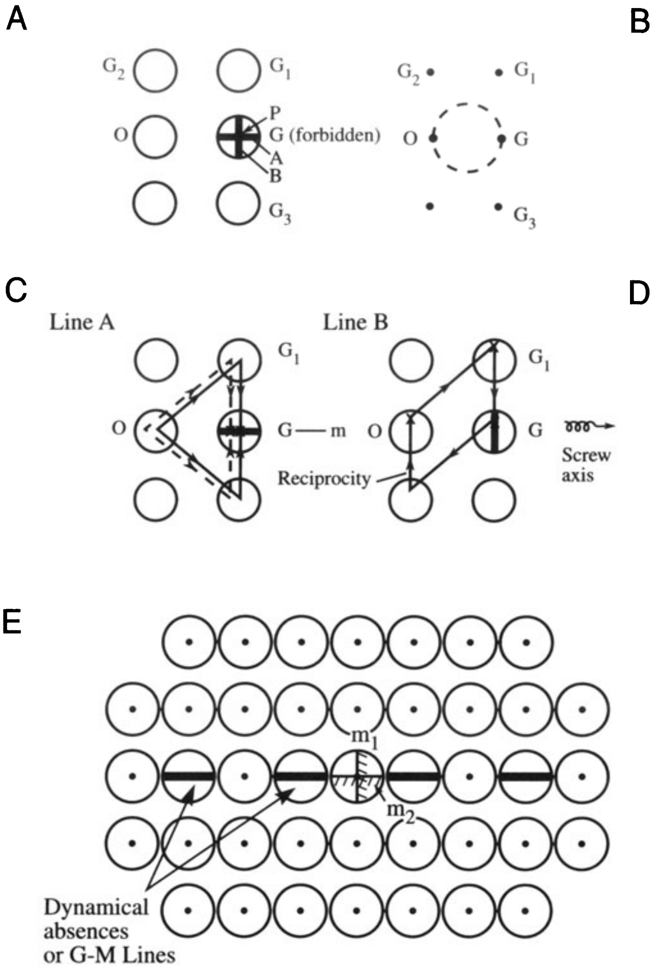

Figure 21.9. The formation of dynamic absences or G–M lines in CBED patterns. In (A) a pair of orthogonal G–M lines form a black cross in a forbidden diffraction disk G. In (B) the position of the Laue circle is shown. In (C) and (D) pairs of diffraction vectors contribute equal and opposite amplitudes, thus causing the lines of dynamic absence. In the ZOLZ of a CBED pattern the G–M lines will occur in alternate reflections, as shown in (E). To determine the translational symmetry elements, examine the orientation of the G–M lines with respect to the BF mirror planes, and consult Table 21.7.

> The dynamical absences are referred to as Gjønnes–Moodie or G–M lines.

As you can see from Table 21.7, you have to carry out an analysis of the orientation of the G–M line with respect to the BF mirrors within the 000 disk, in order to ascertain whether a glide plane, screw axis, or both are present. Once the additional glide planes and screw axes in each orientation are known, and you know the point group, the space group can be identified from Volume A of The International Tables for Crystallography (Hahn 1988) in conjunc-

Table 21.7. The Six Different Cases of Dynamic Absences along a Single Systematic Line of Reflections

Symbols used follow Tables 4.1.6 and 4.1.7 of International Tables for X-ray Crystallography (1969)

WP	BF	Diffraction Group	Orientation of mirrors with respect to lines of absences in a zone-axis pattern (orthogonal lines are principal axes)	Minimum number of symmetry elements responsible for absence
1	*m*	m_R	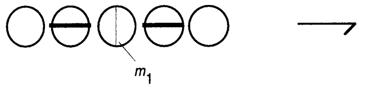	Screw axis perpendicular to beam $2_1 4_1 4_3 6_1 6_3$ or 6_5
	m	$2_R mm_R$ (*a*) and (*b*) or	(*a*) 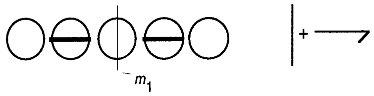	Screw axis perpendicular to the beam and to a mirror plane; $2_1/m$, $6_3/m$
m		*m* (*b*)	(*b*) 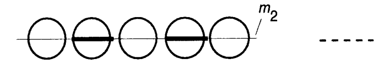	Glide plane parallel to beam
m	2*mm*	$m\,1_R$	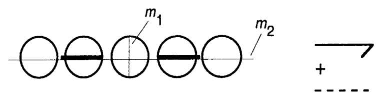	Screw axis (2_1, 6_3) plus parallel glide plane
2*mm*	2*mm*	2*mm* or 2*mm* 1_R	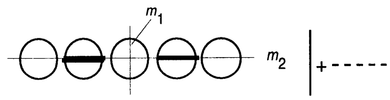	As (*b*) above with an extra mirror plane parallel to the beam and perpendicular to the glide plane
2	2*mm*	$2m_R m_R$	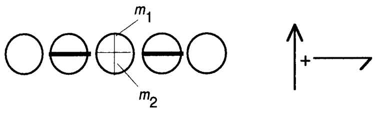	Screw axis ($2_1 4_1 4_3 6_1 6_3$ or 6_5) perpendicular to a 2-fold axis or 2_1 axis perpendicular to a 4-fold axis both perpendicular to the beam

Table 21.7 (continued)
The Seven Cases of Dynamic Absences along Two Orthogonal Lines

WP	BF	Diffraction Group	Orientations of mirrors with respect to lines of absences in zone-axis patterns	Minimum number of symmetry elements responsible for absences
2	2*mm*	$2m_Rm_R$	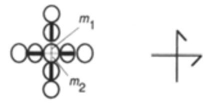	Orthogonal screw axes, orthogonal to the beam direction. 2_1 perpendicular to 2_1, 4_1, or 4_3
2*mm*	2*mm*	2*mm* or $2mm\ 1_R$	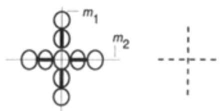	Two perpendicular glide planes
m	*m*	2_Rmm_R	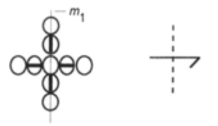	2_1 screw axis perpendicular to a glide plane. (*N.B.* although there are 4_1 screw axes perpendicular to glide plane in cubic *F* and *I* centered space groups dynamic absences do not occur. There are no multiple diffraction routes to the forbidden reflections.)
4	4*mm*	$4m_Rm_R$	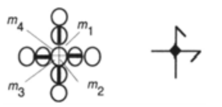	Orthogonal screw diads normal to a tetrad axis (4, 4_1, or 4_3) which is parallel to the beam direction OR an orthogo-nal set of three 4_1 or 4_3 screw tetrad axes with one axisparallel to the beam
2*mm*	4*mm*	4_Rmm_R	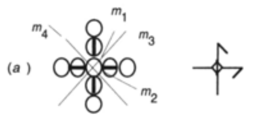	Orthogonal screw diads normal both to an inversion tetrad axis and to the beam direction
			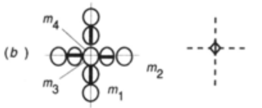	Orthogonal glide planes, parallel to an inversion tetrad axis
4*mm*	4*mm*	4*mm* or $4mm\ 1_R$	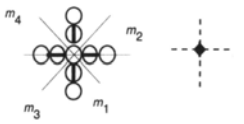	Orthogonal glide planes, parallel both to a tetrad axis (4 or 4_2) and to the beam direction

tion with the rules for forbidden reflections. We can illustrate the determination of translational symmetry elements by observing Figure 21.10 in detail.

Example

$CaZrO_3$ is orthorhombic, with the *mmm* point group. Within the *mmm* point group the only translational symmetry elements allowed are twofold screw/rotation axes and {100} glide/mirror planes. Determination of which translational symmetry elements are present can be deduced by analyzing CBED patterns along <*UV*0> zone axes. These <*UV*0> zone-axis patterns, such as [210], within the *mmm* point group contain only a single BF/WP mirror. Figure 21.10A shows two orthogonal pairs of G–M lines in alternate reflections along the (001), $1 \neq 2n$, and (*hk*0), $h+k \neq 2n$, systematic rows. Figure 21.10D shows the BF disk which displays single mirror symmetry, with (*hk*0), $h+k \neq 2n$ G–M lines being parallel to the bright-field mirror as a consequence of the (001) *c*-glide plane. On the other hand, in the (001) reflection, $1 \neq 2n$ G–M lines, which are normal to the BF mirror, indicate the presence of a twofold screw axis along [001].

Confirmation that these dark bands are in fact G–M lines is given by the observation of "black crosses" when the Bragg reflection condition is satisfied for the forbidden reflections.

For example, Figure 21.10B shows a black cross in (001) and Figure 21.10C shows a black cross in (120). The *mmm* point group, combined with the presence of the *c*-glide plane and the twofold screw axis, permits the space group of $CaZrO_3$ to be determined as *Pcmn*.

21.4. LATTICE PARAMETER, STRAIN, AND COMPOSITION ANALYSIS

We can get a reasonably accurate measurement of the lattice constants (~2%) by indexing the reflections in the ZOLZ and/or by measurement of the HOLZ-ring diameter. However, the best method is to use the positions of HOLZ lines in the BF disk which, because they arise from very high order reflections, are very sensitive to changes in lattice parameter. Results which are an order of magnitude more precise (~0.2%) can be obtained by computer simulation (see Section 20.5) of the position of the HOLZ lines using different lattice constants. The values which produce the best match with the experimentally observed HOLZ-line positions can be identified as the lattice constants of the crystal. So by measuring the HOLZ-line positions we can measure changes in lattice parameters which may occur for a variety of reasons, but materials scientists are most interested in changes due to composition or lattice strain. It is feasible to use this approach to infer, indirectly, the composition of a specimen by comparing the lattice parameter of an unknown with a standard of known composition; in the case of solid solutions, extrapolating to other compositions assuming that Vegard's law applies. Such a chemical analysis is not limited by elemental considerations, as is the case for XEDS, and does not require ultrathin specimens as for EELS. However, it is indirect and makes several assumptions which may not always apply. In addition to composition measurements we can also make very localized measurements of strain around precipitates or defects, but the data are always averaged through the foil thickness, and in one dimension, and so are rather limited.

For determining precise lattice parameters, we compare the experimental HOLZ-line pattern to the computer-simulated version.

In some programs, the position of the HOLZ lines in the simulation is derived from kinematical-diffraction theory only, but dynamical effects which may be important should really be included (Eades *et al.* 1993). The method is:

- Start with a standard specimen of known lattice parameter to establish the exact electron wavelength for subsequent simulations.
- Adjust the continuous kV control. Since you know the lattice parameter, you can determine the exact kV.
- At this predetermined kV setting, obtain a HOLZ-line pattern from the unknown and compare the experimental pattern with simulated patterns generated for a range of lattice parameters, until good matching is achieved between the simulated and experimental patterns (see Figures 21.11A and B). Theoretically, an accuracy of 0.02% should be achievable but in practice an accuracy of 0.2% is generally obtained.

While this approach has demonstrated reasonable success in measuring lattice-parameter shifts as shown by Randle *et al.* (1989), you should be wary of other possible causes of HOLZ-line shifts and the difficulties of exact matching between theory and experiment. Often, the HOLZ-line patterns display asymmetries which make matching impossible. Remember, you need to cool the specimen so you can see HOLZ lines in certain materials. There are some necessary precautions you should take:

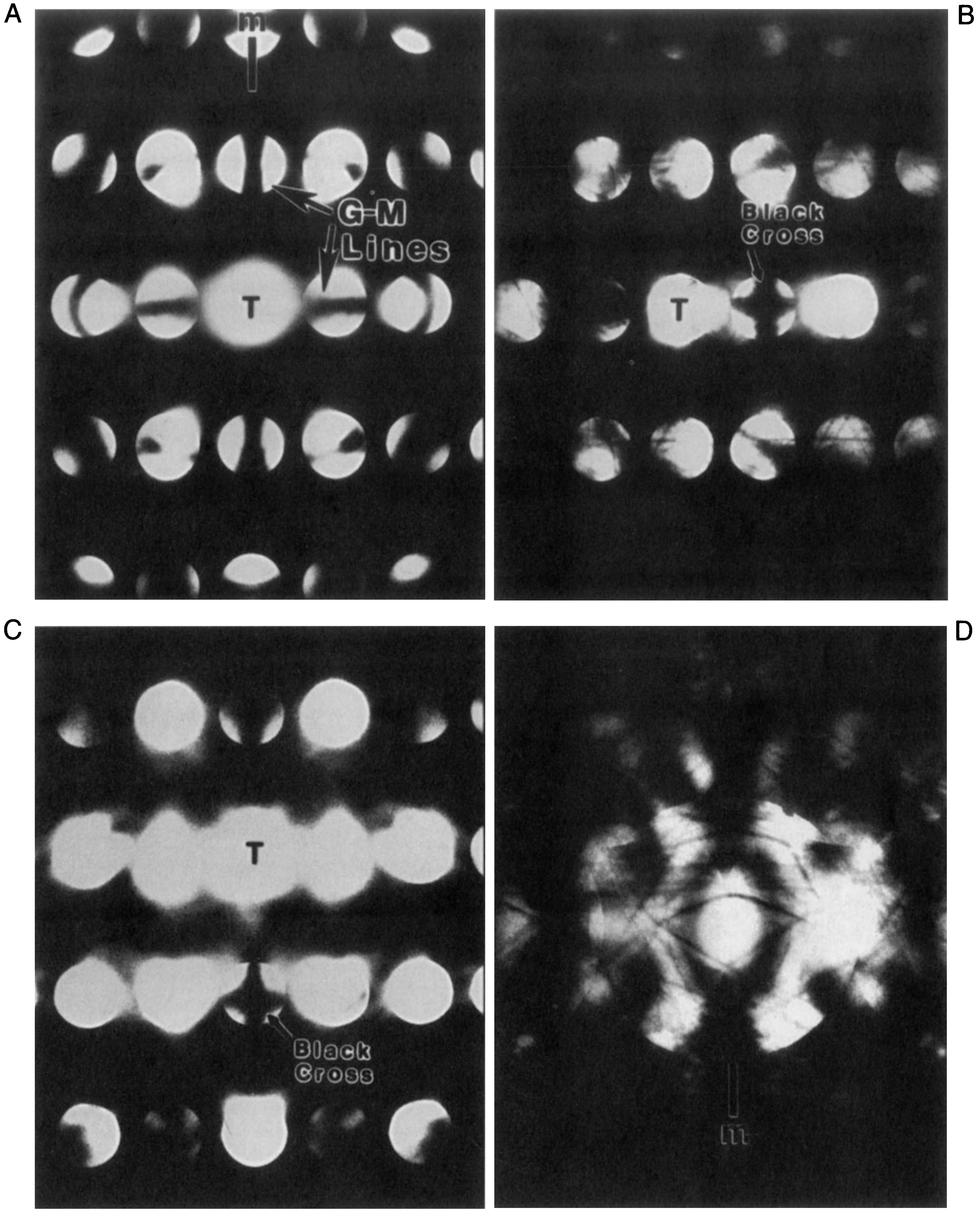

Figure 21.10. The use of G–M lines to determine the space group of $CaZrO_3$ (see text for a full explanation). In (A), orthogonal G–M lines are visible in alternate reflections, while in the (001) reflection (B) and the (120) reflection (C) "black crosses" are visible. In (D) the mirror symmetry is evident, with parallel G–M lines.

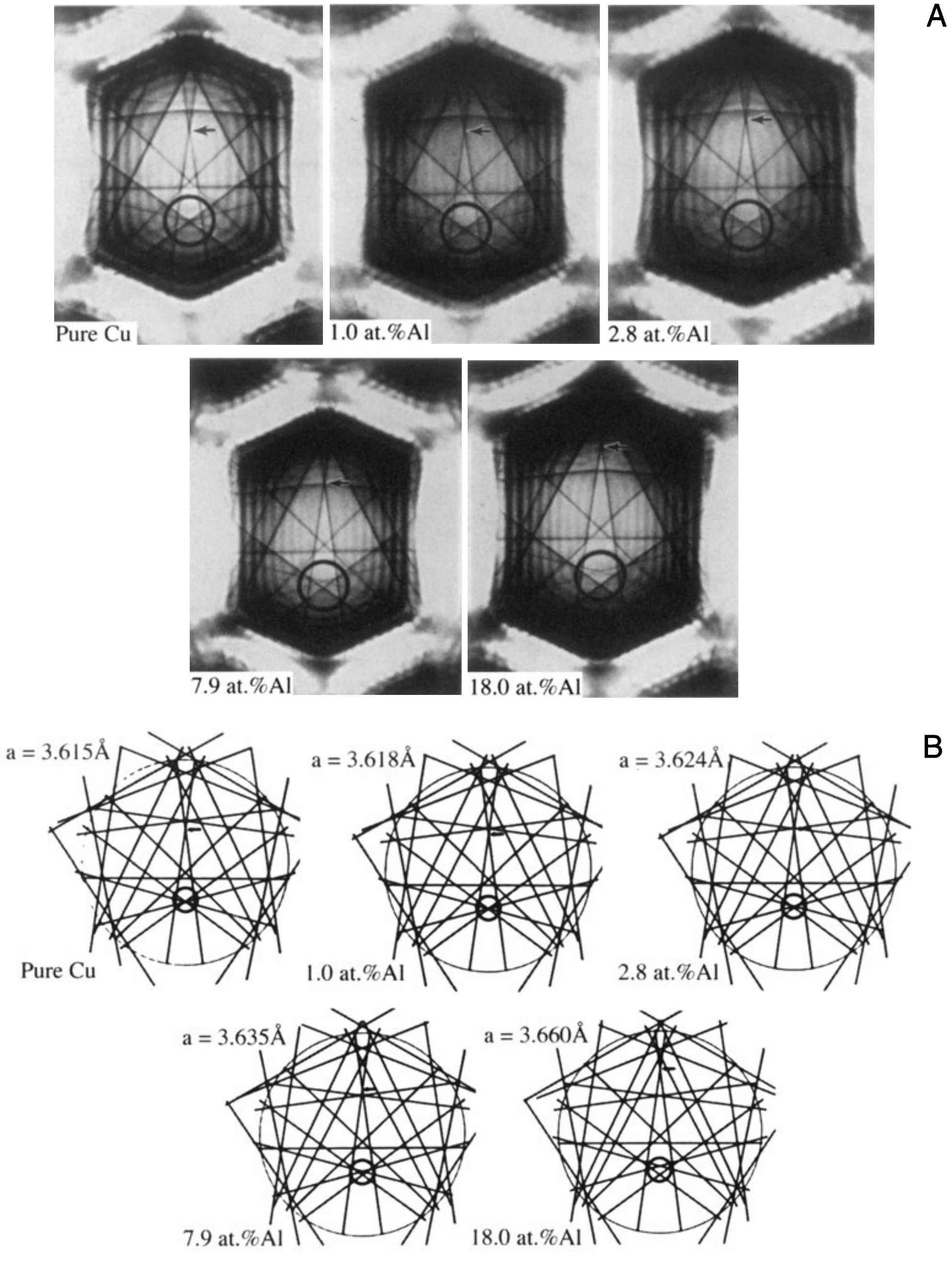

Figure 21.11. (A) HOLZ-line patterns obtained from several different Cu-Al alloys in the [114] orientation at fixed kV. The HOLZ-line shifts are due to changes in lattice parameter. (B) Computer simulation of the HOLZ-line patterns in (A) showing the lattice parameter that corresponds to each experimental pattern.

- Compare your standard and unknown under identical conditions.
- Take account of any differences in thermal contraction coefficient if you cool the specimen to liquid-N_2 temperatures.
- Watch for problems such as surface relaxation, or local strain, or the presence of dislocation lines which can give rise to spurious measurements of lattice parameter.

While this is potentially a very precise technique, its accuracy may be less reliable, so it is probably best not to rely on HOLZ-line shifts as the primary method of absolute lattice parameter or strain determination.

21.5. DETERMINATION OF ENANTIOMORPHISM

Crystals belonging to point groups where only rotation axes are allowed can be either right-handed or left-handed. Another unique aspect of CBED patterns is shown in Figure 21.12. We can use CBED patterns to deduce whether a crystal shows right- or left-handedness, since under these circumstances the pattern symmetries vary depending on which way the beam enters the specimen. Thus, the handedness of a crystal can be readily determined using CBED. If a sample is enantiomorphous (i.e., it has no symmetry elements which change "hand," such as inversion centers or mirrors), then the patterns are different when the beam enters the specimen from opposite directions. So you take patterns before and after turning the specimen upside down. In crystals which do not possess a handedness, CBED patterns obtained with illumination from the top or bottom surface of the crystal are identical. However, in right/left-handed crystals (e.g., quartz) the CBED patterns obtained in this way are no longer identical, but are related to each other by a mirror (or a twofold rotation axis). This is clearly the case in Figure 21.12, which is from enantiomorphous quartz (space group $P3_121$ or $P3_221$).

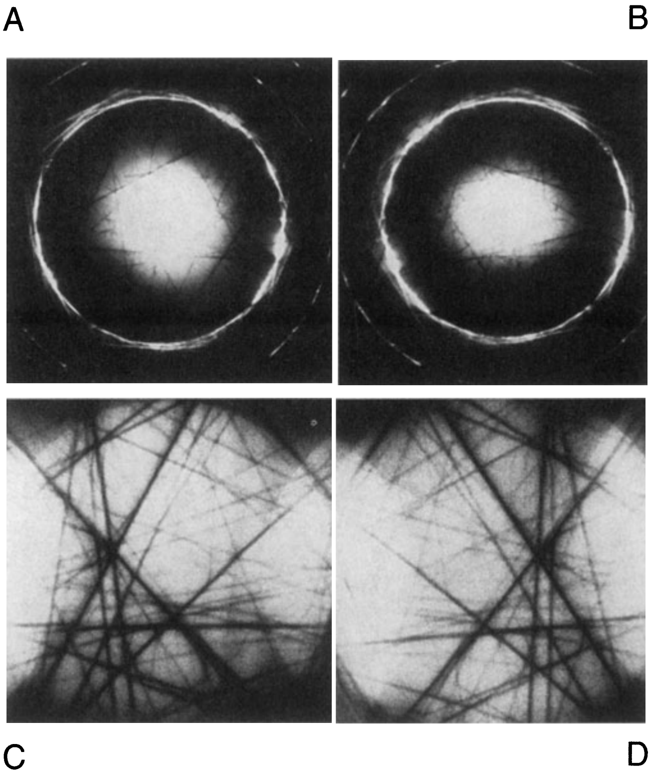

Figure 21.12. (A) and (C) are WP and BF disks, respectively, from a quartz specimen illuminated from the top surface. (B) and (D) are the same patterns, except that the specimen was inverted to illuminate the bottom surface. Note the mirror symmetries between (A) and (B), as well as between (C) and (D).

21.6. CONVERGENT-BEAM IMAGING

You can obtain some direct correlation between CBED symmetry and the image of the specimen. The technique of convergent-beam imaging (CBIM) (Tanaka *et al.* 1988, Humphreys *et al.* 1988) creates a mixture of both image and DP in one. By adjustment of condenser and objective lenses, either the image or the DP can be focused, but not both at the same time.

> **This technique is analogous to the multiple dark-field imaging in TEM in which BF and DF images are visible in defocused SAD patterns (see Figure 9.25).**

CBIM is carried out by focusing the convergent beam either above or below the specimen plane, in which case HOLZ lines are projected, although somewhat broadened, into the normal image plane. So you should use the smallest possible probe, with reasonable defocus values; then the HOLZ-line resolution, governed by the probe size, remains acceptable. This technique has the advantage that your image resolution is that expected from the microscope under normal diffraction-contrast conditions. For example, in Figure 21.13, the change in symmetry across a two-phase interface between NiO and CaO is clearly visible, as is the diffraction contrast associated with the interface. The insets show a TEM image of the interface and an SAD pattern across the interface showing the orientation relationship between the phases.

21.7. SCANNING-BEAM DIFFRACTION

Diffraction phenomena can be imaged in scanning-beam instruments, just as in TEM. For example, the phenomenon of electron channeling is one way to obtain crystallographic information from a bulk crystal in the SEM. This technique is somewhat outside the scope of this book; however, channeling is possible in a STEM or DSTEM and channeling patterns contain similar HOLZ information as CBED patterns. If you're interested you should look up any standard SEM text.

Scanning-diffraction patterns are obtainable in STEMs using either one or two sets of coils both before

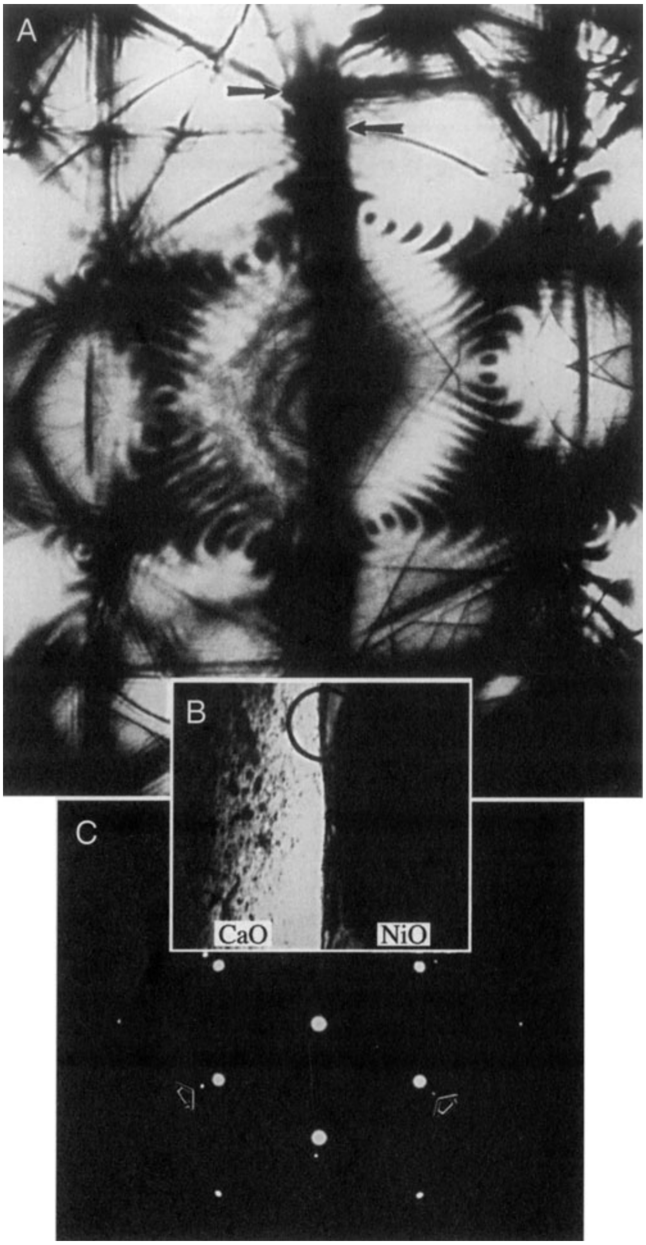

Figure 21.13. (A) CBIM pattern of a NiO-CaO eutectic interface (B). In this directionally solidified eutectic all directions and planes in both phases are parallel to each other, as evident in the SAD pattern (C). The CBIM pattern displays the parallelism of (220) mirror planes which are normal to the planar interface, and the lack of continuity of HOLZ lines and Kikuchi bands indicates the lattice mismatch across the interface.

and after the specimen. In both cases the beam is stationary at the plane of the specimen and rocks back and forth in a manner similar to the rocking-beam method of microdiffraction (see Section 21.8). Using only one scan coil below the specimen partially "de-rocks" the beam, but two coils

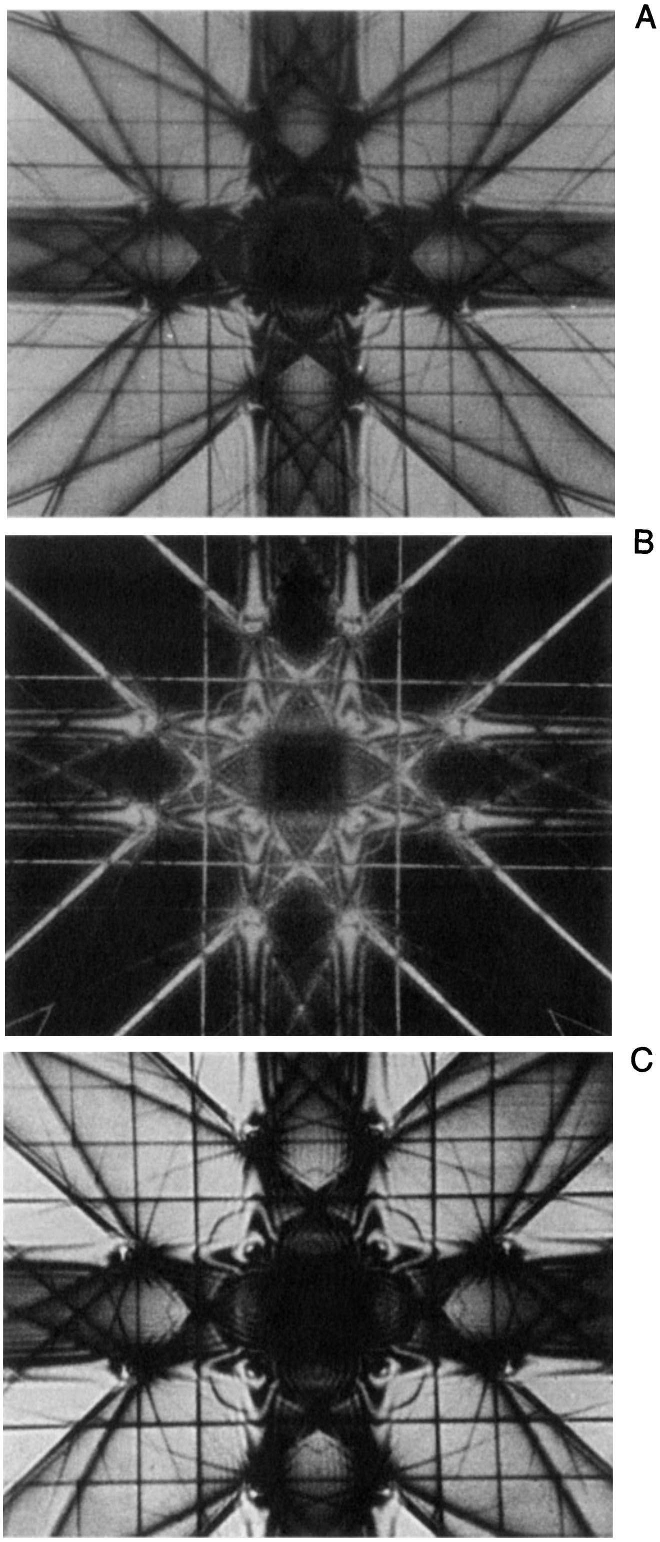

Figure 21.14. A series of Eades double-rocking zone-axis patterns obtained from a thin sample of aluminum in the [001] orientation. (A) is the BF image, (B) is a DF image, and (C) is an energy-filtered version of (A). The removal of energy-loss electrons sharpens the image.

fully "de-rock" the beam such that, instead of having the DP scan across the BF STEM detector, the 000 disk is always on the optic axis and thus on the BF detector. However, the HOLZ lines, etc., move continuously across the detector because, like Kikuchi lines, they are "fixed" to the specimen. The resulting patterns cover several degrees in comparison with the fractions of a degree visible in a normal CBED disk. The resultant patterns are very striking, as you can appreciate from Figure 21.14; such patterns can be viewed in BF or DF. In addition, the images can be sharpened by sending the electrons through an energy filter (Figure 21.4C) prior to displaying the pattern on the CRT (see Chapter 40). These approaches can be used to study the occurrence of forbidden reflections, which are important in crystal-symmetry determinations.

Grigson scanning is a method of obtaining DPs in a DSTEM without any post-specimen lenses. In such an instrument, the DP is only visible if it is scanned across the STEM detector and displayed on the CRT. In a DSTEM with an FEG source but no post-specimen lenses, the pattern is viewed by stopping the scan and positioning the beam on the area of interest. With an FEG, DPs can be obtained from subnanometer-diameter regions if the specimen is thin enough. The Grigson method is highly inefficient and collects only a small fraction of the DP at a time: it's a serial technique. More usually, in a DSTEM the pattern is viewed directly from a TV recording of the back focal plane of the objective lens. Almost always, post-specimen lenses are now included in a DSTEM to allow you to use a range of camera lengths. This method of very high resolution microdiffraction, sometimes termed "nanodiffraction," has been pioneered by Cowley and co-workers (Cowley 1981). Figure 21.15 shows a sequence of DPs obtained across a single carbon nanotube.

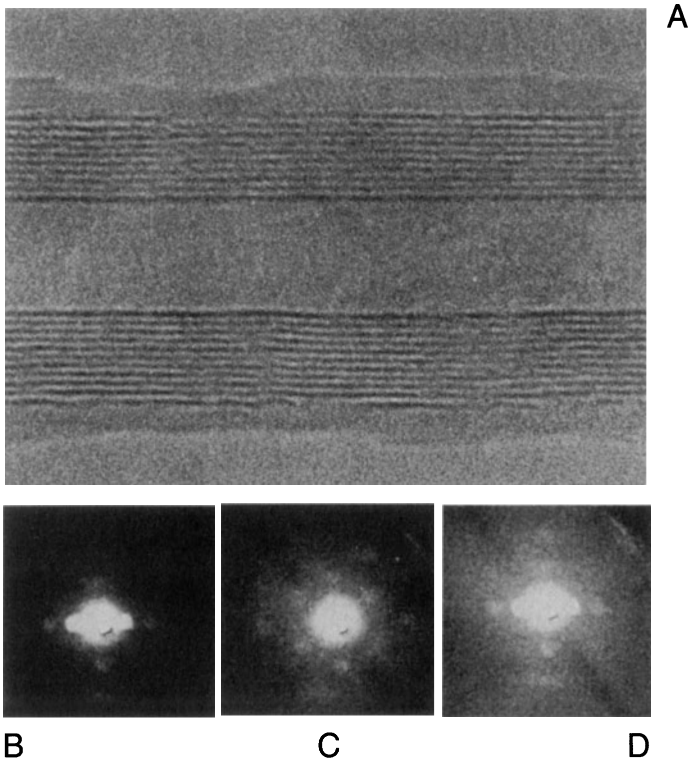

Figure 21.15. (A) A single carbon nanotube of circular cross section and zero helix angle. The 0.34-nm 0002 graphite lattice fringes are clearly resolved. (B–D) Nanodiffraction patterns taken from the upper, center, and lower regions of the nanotube, respectively.

21.8. OTHER METHODS OF MICRODIFFRACTION

It is possible to obtain microdiffraction patterns in TEMs and STEMs by methods other than CBED, although no other technique combines the versatility and ease of CBED. The need for diffraction information from below the SAD limit was originally addressed by Riecke (1962). He developed a strong C3 lens, or mini-lens, which permitted a large demagnification of the C2 aperture onto the specimen. While this approach was similar to SAD, the available demagnification was much larger. However, the state of development of electron optics at that time was such that, to get the best area selection, it was necessary to operate with the specimen raised above the eucentric plane, which meant that few users were prepared to try the technique. This limitation has been overcome with the development of condenser-objective lenses and the Riecke method can still be used to produce patterns from regions of a few tens of nanometers in diameter. In a modern TEM the equivalent method is often called "nanoprobe" mode. You first create a fine probe in TEM mode with a small C2 aperture, defocus the probe to give parallel illumination, then switch to diffraction mode to view the pattern. Because these patterns are obtained with a parallel beam the diffraction spots are points, not disks, and an example is shown in Figure 21.16.

With the development of STEMs, it became possible to obtain diffraction information in a unique manner by using the scan coils to rock the beam through a range of angles above the specimen. This "rocking-beam" method has been refined to the point where patterns from regions below 5 nm are obtainable. The pattern is created by the varying intensity that falls on the STEM BF detector as the beam changes its angle of incidence to the spec-

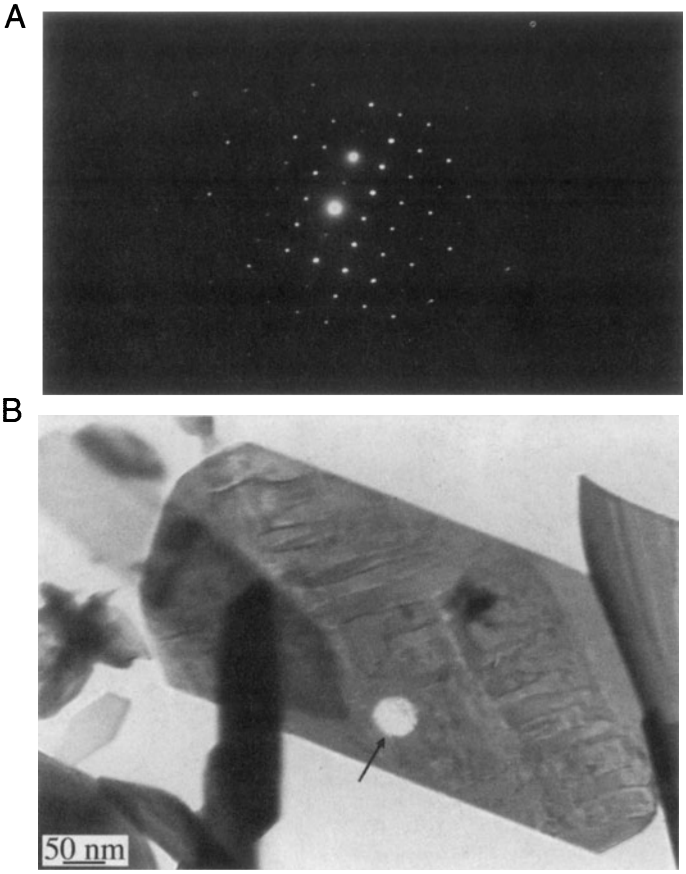

Figure 21.16. (A) A Riecke diffraction pattern from a single crystal of MoO_3. (B) A double exposure of the crystal and the bright area (arrowed) illuminated by the small parallel beam. The pattern is identical to an SAD pattern except that it comes from a region of ~50-nm diameter.

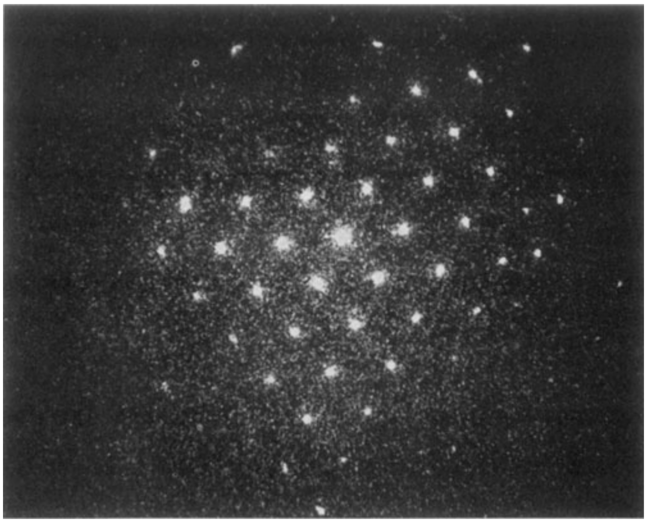

Figure 21.17. Rocking-beam pattern of graphitized carbon from the CRT screen of a DSTEM.

imen, and is recorded on the STEM CRT. In a DSTEM, such patterns are also useful to determine the collection angle of the EELS spectrometer, and an example of a rocking-beam pattern is shown in Figure 21.17. Neither Riecke nor rocking-beam techniques are extensively used. They are historically interesting, but do not compete in any way with CBED, which is by far the best method of obtaining crystallographic information about your specimen.

CHAPTER SUMMARY

CBED patterns contain contrast information which can be used to give the point group, space group, crystal system, and lattice parameter of very small crystals, as well as other information such as thickness and enantiomorphism. To do this requires some detailed knowledge of crystal-symmetry concepts, stereographic projections, and the ability to produce ZAPs from a variety of orientations. In addition, the determined operator is often rewarded with patterns that are both very useful and stunningly beautiful. If you want to determine the point group, you need to obtain from your CBED patterns:

- WP symmetry.
- BF symmetry.

These symmetries lead you to the diffraction group, which describes the full 3D symmetry of a DP and is directly related to the point group through Buxton's tables.

If you successfully worked your way through these two chapters, then you're ready for the more challenging aspects of CBED, such as measurement of structure factors, Debye–Waller factors, and charge density discussed in the text by Spence and Zuo (1992).

REFERENCES

General References

Eades, J.A. (1988) *Ultramicroscopy* **24**, 143.

Eades, J.A., Ed. (1989) *J. Electron Microsc. Tech.* **13** (I & II). Special issues on CBED.

Loretto, M.H. (1994) *Electron Beam Analysis of Materials,* 2nd edition, Chapman and Hall, New York.

Mansfield, J.F. (1984), *Convergent Beam Electron Diffraction of Alloy Phases,* Adam Hilger, Bristol, United Kingdom.

Spence, J.C.H. and Zuo, J.M. (1992) *Electron Microdiffraction*, Plenum Press, New York. You will want a copy of this if you use CBED extensively. The code for plotting HOLZ lines is included in the appendices along with the Fortran code for two programs, one Bloch wave and one multislice. You may also find a reference to earlier CBED studies on your material here in the selective bibliography organized by material.

Sung, C.M. and Williams, D.B. (1991) *J. Elect. Microsc. Tech.* **17**, 95. A bibliography of CBED papers from 1939–1990.

Tanaka, M. and Terauchi, M. (1985) *Convergent Beam Electron Diffraction,* JEOL, Tokyo.

Tanaka, M., Terauchi, M., and Kaneyama, T. (1988) *Convergent Beam Electron Diffraction,* **II**, JEOL, Tokyo.

Specific References

Allen, S.M. (1981) *Phil. Mag.* **A43**, 325.

Ayer, R. (1989) *J. Electron Microsc. Tech.* **13**, 16.

Buxton, B.F., Eades, J.A., Steeds, J.W., and Rackham, G.M. (1976) *Phil. Trans. Roy. Soc.* **281**, 181.

Cowley, J.M. (1981) *Ultramicroscopy* **7**, 19.

Eades, J.A., Moore, S., Pfullman, T., and Hangas, J. (1993) *Microscopy Research and Technique* **24**, 509.

Gjønnes, J. and Moodie, A.F. (1965) *Acta Cryst.* **19**, 65.

Hahn, T., Ed. (1988) *International Tables for Crystallography,* A. *Space-group Symmetry,* Kluwer Academic Publisher, Norwell, Massachusetts.

Hirsch, P.B., Howie, A., Nicholson, R.B., Pashley, D.W., and Whelan, M.J. (1977) *Electron Microscopy of Thin Crystals,* 2nd edition, p. 122, Krieger, Huntington, New York.

Humphreys, C.J., Maher, D.M., Fraser, H.L., and Eaglesham, D.J. (1988) *Phil. Mag.* **58A**, 787.

Jackson, A.G. (1987) *J. Electron Microsc. Tech.* **5**, 373.

Jackson, A.G. (1990) *Ultramicroscopy* **32**, 181.

Kelly, P.M., Jostons, A., Blake, R.G., and Napier, J.G. (1975) *Phys. stat. sol.* **A31**, 771.

Raghavan, M., Scanlon, J.C., and Steeds, J.W. (1984) *Met. Trans.* **15A**, 1299.

Randle, V., Barker, I., and Ralph, B. (1989) *J. Electron Microsc. Tech.* **13**, 51.

Riecke, W.D. (1962) *Proc. 5th Int. Cong. on Electron Microscopy,* **1** (Ed. S.S. Breese Jr.), p. KK-5, Academic Press, New York.

Steeds, J.W. (1979) *Introduction to Analytical Electron Microscopy* (Eds. J.J. Hren, J.I. Goldstein, and D.C. Joy), p. 387, Plenum Press, New York.

Steeds, J.W. (1984) "Electron Crystallography," in *Quantitative Electron Microscopy,* (Eds. J.N. Chapman and A.J. Craven), p. 49, Scottish Universities Summer School in Physics, Edinburgh.

Steeds, J.W. and Vincent, R. (1983) *J. Appl. Cryst.* **16**, 317.

Tanaka, M. (1989) *J. Electron Microsc. Tech.* **13**, 27.